Heliospheric regimes governing Forbush decreases revealed by multiscale analysis of cosmic rays

D. Sierra-Porta[a] and C. Varotsos[b,*]

[a]Universidad Tecnológica de Bolívar, Grupo de Investigación Gravitación y Matemática Aplicada - GIGMA & Grupo de Investigación Física Aplicada y Procesamiento de Imágenes y Señales - FAPIS. Parque Industrial y Tecnológico Carlos Vélez Pombo Km 1 Vía Turbaco, Cartagena de Indias, 130010, Bolívar, Colombia
[b]National and Kapodistrian University of Athens, Faculty of Physics, 15784 Athens, Greece
[*]Corresponding author: email: covar@phys.uoa.gr

Abstract

We investigate the dynamical structure of galactic cosmic ray intensity using multiscale analysis applied to daily records from 16 neutron monitor stations over 2010–2025. The objective is to determine whether large Forbush decreases are associated with identifiable statistical states of heliospheric modulation. We identify a statistically distinct heliospheric regime—characterised by elevated long-range persistence and reduced natural-time variance—in which large Forbush decreases are significantly more likely. Multifractal detrended fluctuation analysis and natural time analysis are applied in a rolling framework to characterize long-range correlations and event-order dynamics. The results show that persistent long-range correlations and multifractal structure are universal across the global network. A coherent evolution driven by the solar cycle is observed, with reduced persistence during the 2019–2020 solar minimum and enhanced organization during active periods. Across nine major Forbush decreases, 78% occur during intervals of elevated persistence and reduced natural-time variance, indicating a distinct heliospheric regime associated with an increased likelihood of events. No significant relationship is found between these metrics and event magnitude, confirming that the signal reflects a statistical state rather than a deterministic precursor. The combined analysis demonstrates that multiscale and natural-time approaches provide complementary information, offering a more complete characterization of heliospheric dynamics and reframing Forbush decreases as regime-dependent phenomena rather than isolated stochastic events.

Keywords: cosmic rays; multifractal analysis; natural time analysis; Forbush decreases; heliospheric modulation; neutron monitors

1 Introduction

Galactic cosmic rays (CRs) are relativistic charged particles of extra-solar origin whose intensity at Earth is continuously modulated by the heliospheric magnetic field. As solar activity varies over the 11-year cycle, the expanding solar wind creates a time-varying magnetic barrier that partially shields the inner heliosphere from the galactic CR flux [1–3]. Superimposed on this background modulation, transient events such as interplanetary coronal mass ejections (ICMEs) and their associated magnetic sheaths produce sharp, temporary decrements in cosmic ray intensity (CRI) known as Forbush decreases [4–6]. The detection, characterisation, and physical interpretation of Forbush decreases are central problems in space weather research, both for understanding heliospheric plasma dynamics and for assessing the radiation environment in near-Earth space [7].

Experiments from the CERN CLOUD project have further shown that cosmic-ray-induced ionization enhances the nucleation of ultrafine aerosol particles, strengthening the link between cosmic-ray variability and atmospheric aerosol formation [8–10].

The temporal structure of CRI variations is far from random. Ground-based measurements from the global neutron monitor network [7] reveal persistent long-range correlations spanning timescales from days to years, which cannot be accounted for by short-memory stochastic processes alone. Several physical mechanisms can produce such correlations in the CR flux: self-organised critical dynamics in the heliospheric plasma [7], long-memory stochastic processes such as fractional Gaussian noise [11], turbulent cascades in the solar wind consistent with the Kolmogorov–Obukhov scaling [7], or multi-scale transport effects arising from diffusion in a structured magnetic field [3, 12–15]. Discriminating between these mechanisms requires analytical tools that can characterise both the amplitude scaling and the temporal ordering of CR fluctuations. Recent multifractal analyses of solar wind magnetic field fluctuations have confirmed that nonlinear current sheets and intermittent turbulent structures are the primary source of multifractality in the heliospheric plasma [16, 17], motivating their systematic characterisation in the ground-based CR record that reflects this upstream variability.

Detrended Fluctuation Analysis (DFA) and its multifractal generalization (MF-DFA) [18, 19] are now well-established tools for quantifying long-range scaling in non-stationary time series. In the context of CRs, MF-DFA has demonstrated that CRI exhibits genuine multifractal behavior whose degree, measured by the singularity spectral width $\Delta\alpha$, is modulated by geomagnetic cut-off rigidity [20, 21] varies systematically with heliospheric activity [22], and is sensitive to the occurrence of geomagnetic storms [23], with scaling exponents showing systematic dependence on solar cycle phase [24]. These studies, however, have been predominantly static or limited to a small number of stations, and no systematic rolling MF-DFA analysis at the global network scale had been attempted before this work. Beyond cosmic ray applications, MF-DFA-based approaches have proven effective in characterising multi-scale dynamics across a range of geophysical time series, from hydroclimatic records to atmospheric trace gases [25–29], underscoring the generality of the framework adopted here.

The broader family of complexity and nonlinear time series methods — including permutation entropy, Lempel–Ziv complexity, and fractal dimension estimators — has increasingly been applied to solar wind and geomagnetic data to characterise the distinct dynamical signatures of different heliospheric structures [17, 30]. Within this landscape, MF-DFA and NTA occupy complementary niches: MF-DFA quantifies the amplitude-scaling hierarchy of fluctuations, while NTA reweighs the event sequence by energy content, probing aspects of the dynamics that entropy-based measures do not capture [31]. Applying both frameworks simultaneously to the same CR data windows allows, for the first time, a direct empirical comparison of their information content in the context of heliospheric modulation.

An entirely different perspective on CR dynamics is offered by Natural Time Analysis (NTA), introduced by Varotsos et al. [32] as a framework for studying complex systems by focusing on the order and energy content of events rather than conventional clock time. In NTA, each measurement k is assigned the normalised index $\chi_k = k/N$ and an energy weight $p_k = Q_k/\sum Q_n$; the variance of natural time $\kappa_1 = \langle\chi^2\rangle - \langle\chi\rangle^2$ serves as a measure of the distance from criticality, with $\kappa_1 \to 0.070$ at the critical state [32]. NTA was recently extended to CRs analysis by Varotsos [7], who showed that the entropy in natural time is maximised in concert with the Kolmogorov–Obukhov scaling law, and who reported NTA-based signatures approaching criticality in the hours preceding the extreme May

2024 Forbush decrease. Varotsos et al. [33] further demonstrated that the power spectral density of the CR time evolution obeys the $\gamma = 5/3$ Kolmogorov–Obukhov law, providing a direct connection between turbulence-cascade theory and the NTA entropy maximum.

Despite their distinct mathematical foundations — MF-DFA operates in amplitude–scale space, characterising the hierarchy of fluctuation sizes across temporal scales, while NTA operates in event-order space, characterising the energy distribution of the event sequence — both frameworks have been shown to carry physically meaningful information about the CR system. Whether they capture the same or complementary aspects of the underlying dynamics has never been systematically investigated. Equally absent from the literature is a dynamic, rolling analysis of multifractal parameters across the full global neutron monitor network, which would reveal whether the scaling structure of CRI evolves coherently in space and time in response to heliospheric forcing.

This paper addresses these gaps. Extending the two-station analysis of Varotsos [7] to 16 stations of the Neutron Monitor Database (NMDB; [14]) over 2010–2025, we apply MF-DFA in both static and rolling configurations and combine the results with a parallel rolling NTA applied to the same data windows. We stress at the outset that we do not claim to identify deterministic precursors of individual Forbush decreases. Rather, our central finding is the identification of a statistical dynamical regime of the heliosphere — characterised by elevated CR persistence ($h(2) > 1.05$) and reduced NTA variance ($\kappa_1 < 0.082$) — in which large Forbush events are systematically more likely. This regime is detected independently by both analytical frameworks across nine major events spanning two solar cycles, providing mutual validation of its physical reality. The 2010–2025 study period was selected specifically because it spans the full declining phase of solar cycle 24, the deep 2019–2020 solar minimum, and the rising and maximum phases of solar cycle 25, thereby capturing contrasting heliospheric conditions within a single, internally consistent dataset and enabling a direct test of whether the identified multifractal and natural-time signatures track solar-cycle phase.

Specifically, this paper makes the following novel contributions to the CRs and space weather literature: (i) the first network-scale, time-evolving multifractal characterization of CRI across 16 stations of the NMDB, confirming the universality of $1/f$-type persistence across all latitudes, altitudes, and geomagnetic rigidities; (ii) the identification of a coherent network-wide multifractal response to the solar cycle and to individual Forbush decrease events, revealed by a superposed epoch analysis of nine catalogued events; (iii) the first simultaneous rolling application of MF-DFA and NTA to identical data windows, enabling a direct empirical comparison of amplitude-scale and event-order representations, quantifying empirically that the two frameworks are complementary rather than redundant ($r^2 \approx 1.4\%$ shared variance); and (iv) a case study of anomalous spectral-width behaviour at Jungfraujoch in the months preceding the two extreme 2024 Forbush events — presented as an illustrative signal that does not generalise statistically across the full event catalogue, but whose physical interpretation suggests rigidity-dependent sensitivity to early heliospheric restructuring.

We emphasize that no short-term predictive capability is claimed: the identified regime operates on multi-month timescales and modulates the likelihood of events rather than triggering individual Forbush decreases. The objective of this study is to identify whether large Forbush decreases are associated with statistically distinct heliospheric regimes rather than deterministic precursors.

The paper is organized as follows. Section 2 describes the data, preprocessing pipeline, and methods. Section 3 presents results in five subsections including static network characterization, dynamic evolution and network-wide coherence, case-study spectral-width behaviour, the NTA–MF-DFA bridge, and the multi-event analysis. Section 4 discusses the physical interpretation and limitations. Section 5 summarises the conclusions and outlines future directions.

2 Data and Methods

2.1 Observational Data

Daily mean CRI data were obtained from the Neutron Monitor Database (NMDB; https://www.nmdb.eu), a publicly accessible, globally distributed archive of real-time and historical neutron monitor (NM) measurements [14]. The NMDB provides pressure-corrected count rates with temporal resolutions as fine as one minute; in this study, we use daily means derived from the one-hour validated resolution records.

The analysis covers the period from 1 January 2010 to 30 November 2025, spanning approximately 15.9 years and encompassing portions of solar cycles 24 and 25. From the full NMDB network, we selected stations satisfying two criteria: (i) continuous operation throughout the study period and (ii) a fraction of missing daily values below 5%. This yielded 17 candidate stations. One additional station, Moscow (MOSC), was subsequently excluded due to a documented level-shift in its count rate around 2016, likely attributable to an instrumental recalibration, which persisted after detrending and introduced spurious scaling behaviour in the multifractal analysis (see Section 2.2). Because MF-DFA estimates scaling exponents from the statistics of detrended fluctuations, an abrupt, uncorrected level-shift introduces an artificial low-frequency component that inflates apparent persistence independently of genuine heliospheric signal. Retaining MOSC would therefore have biased both the station-level estimate for Moscow and, given the network-wide averaging used in Section 3.1.2, the reported network mean ($\langle h(2) \rangle$). Its exclusion ensures that the reported network-level statistics reflect genuine heliospheric persistence rather than an instrumental artefact at a single station. The final dataset thus comprises 16 stations spanning a wide range of geomagnetic cut-off rigidities (R_c) and geographic latitudes, as summarised in Table 1.

Table 1: NMDB stations used in this study, with geomagnetic cut-off rigidity R_c. MOSC was excluded from the final analysis (see text).

Code	**Station**	**Lat.**	**Lon.**	**Alt. (m)**	R_c **(GV)**
AATB	Alma-Ata B, Kazakhstan	43.25°N	76.60°E	3340	6.69
APTY	Apatity, Russia	67.57°N	33.40°E	181	0.65
ATHN	Athens, Greece	37.97°N	23.78°E	260	8.53
BKSN	Baksan, Russia	43.28°N	42.69°E	1700	5.60
FSMT	Fort Smith, Canada	60.02°N	111.93°W	180	0.30
INVK	Inuvik, Canada	68.36°N	133.72°W	21	0.30
JUNG	Jungfraujoch (IGY), Switzerland	46.55°N	7.98°E	3570	4.49
JUNG1	Jungfraujoch (NM64), Switzerland	46.55°N	7.98°E	3475	4.49
KERG	Kerguelen Island, France	49.35°S	70.25°E	33	1.14
MXCO	Mexico City, Mexico	19.33°N	99.18°W	2274	8.28
NAIN	Nain, Canada	56.55°N	61.68°W	46	0.30
NEWK	Newark, USA	39.68°N	75.75°W	50	2.40
OULU	Oulu, Finland	65.05°N	25.47°E	15	0.81
PSNM	Doi Inthanon, Thailand	18.59°N	98.49°E	2565	16.8
SOPO	South Pole, Antarctica	90.00°S	0.00°E	2820	0.10
THUL	Thule, Greenland	76.60°N	68.70°W	26	0.30
MOSC*	Moscow, Russia	55.47°N	37.32°E	200	2.43

*Excluded due to an instrumental level-shift around 2016.

Two geomagnetic storms and Forbush decrease events serve as the primary targets of the dynamic analysis:

- *24 March 2024* — a moderate geomagnetic storm (Dst≈ -200 nT) accompanied by a Forbush decrease, associated with active-region flares and a coronal mass ejection [7].
- *10–11 May 2024* — the strongest geomagnetic storm since 2003 (Dst$= -412$ nT, $K_p \approx 9$), producing a pronounced Forbush decrease detected by neutron monitors worldwide, with solar wind speed peaking near 989 km s^{-1} [7].

2.2 Data Preprocessing

Raw daily CRI records were subjected to a three-step preprocessing pipeline before multifractal analysis, applied independently to each station (Fig. 1).

Step 1 – Gap filling. Missing values representing gaps of up to 10 consecutive days (consistent with the $< 5\%$ overall criterion) were filled by linear interpolation. Isolated missing values at the boundaries of the record were filled by forward and backward propagation.

Step 2 – Local outlier removal. Isolated spikes, particularly prominent in stations with low absolute count rates such as ATHN, were identified using a 30-day rolling median and rolling standard deviation. Values deviating by more than three local standard deviations from the rolling median were flagged and replaced by linear interpolation between their nearest valid neighbors. This criterion removes single-day instrumental or data-transmission artefacts while preserving the characteristic rapid-recovery profile of genuine Forbush decreases, which unfold over 7–14 days.

Step 3 – Solar-cycle detrending and normalisation. The slowly varying background modulation driven by the $\sim$11-year solar activity cycle was removed by subtracting a 365-day centred rolling mean from each station's record. This choice of window is long enough to capture the quasi-annual modulation of the galactic CR flux without distorting shorter-term transients. As a by-product, the detrending effectively absorbs the level-shift identified in MOSC around 2016, which is why that station was retained to this stage for diagnostic purposes before final exclusion. After detrending, each series was expressed as a percentage anomaly relative to its station mean:

$$x_i' = \frac{x_i - \bar{x}_{\text{trend}}(i)}{\bar{x}} \times 100, \tag{1}$$

where $\bar{x}_{\text{trend}}(i)$ is the 365-day rolling mean, and $\bar{x}$ is the long-term station mean computed before detrending. This normalisation renders series from different stations dimensionless and directly comparable, as it removes the dependence on detector size and atmospheric depth that causes raw count rates to differ by orders of magnitude across the network.

The preprocessing pipeline was validated visually for each station. For ATHN, JUNG, and APTY, the resulting anomaly series show zero mean, bounded ranges of $\pm$6–10%, and no residual secular trend, confirming the effectiveness of the procedure (Fig. 1).

2.3 Multifractal Detrended Fluctuation Analysis

To investigate the scaling properties and multifractal structure of the preprocessed CRI series, we employed Multifractal Detrended Fluctuation Analysis (MF-DFA), following the formulation of Kantelhardt et al. [19]. MF-DFA generalizes the standard DFA [18] to arbitrary moment orders q, thereby capturing the full spectrum of scaling exponents present in the data.

For a time series of length N, the procedure is as follows. The integrated profile $Y(i) = \sum_{k=1}^{i}[x(k) - \langle x \rangle]$ is divided into $N_s = \lfloor N/s \rfloor$ non-overlapping segments of length s. In each segment a local polynomial trend (here of order $m = 2$, i.e. DFA2, matching Varotsos 7) is estimated by least squares and subtracted. The q-th order fluctuation function is then computed as

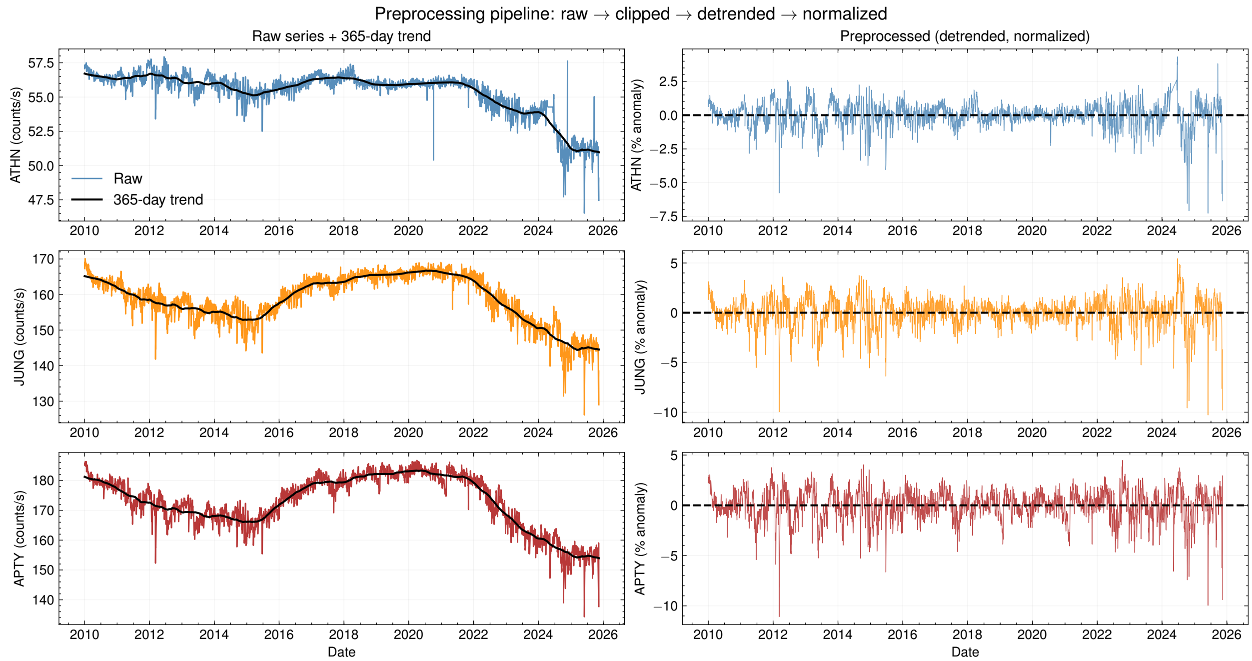

Figure 1: Preprocessing pipeline applied to three representative stations. Left column: raw daily CRI (blue/orange/red) with the superimposed 365-day centred rolling mean (black), used for solar-cycle detrending. Right column: resulting anomaly series expressed as percentage deviations from the station mean. From top to bottom: Athens (ATHN), Jungfraujoch IGY (JUNG), and Apatity (APTY). The detrending effectively removes the secular modulation driven by the ~11-year solar cycle while preserving shorter-term transients, including Forbush decreases.

$$F_q(s) = \left\{ \frac{1}{N_s} \sum_{\nu=1}^{N_s} \left[F^2(\nu, s) \right]^{q/2} \right\}^{1/q}, \qquad q \neq 0, \tag{2}$$

where $F^2(\nu, s)$ is the mean-squared residual in segment ν. For $q = 0$ the geometric mean is used. If long-range power-law correlations are present, $F_q(s) \sim s^{h(q)}$, where $h(q)$ is the generalised Hurst exponent. The classical Hurst exponent corresponds to $h(2)$; values $h(2) > 0.5$ indicate persistent long-range correlations and $h(2) \approx 1$ characterises $1/f$ (pink) noise.

For the static (whole-series) analysis we used segment sizes spanning 2^3 to 2^{10} days (8–1024 days) with 15 logarithmically spaced values, and moment orders $q \in [-5, 5]$ in steps of 0.25. The multifractal spectrum $f(\alpha)$ was obtained from $h(q)$ via the Legendre transform. The spectral width

$$\Delta\alpha = \alpha_{\max} - \alpha_{\min} \tag{3}$$

quantifies the degree of multifractality: $\Delta\alpha = 0$ for a monofractal signal and larger values indicate a richer multifractal structure. Only values from the physically valid range of the spectrum ($f(\alpha) \geq -0.5$) were retained to avoid numerical instabilities at the spectral tails. The spectral asymmetry was not considered because its estimation proved numerically unreliable for detrended daily CR records, where the denominator of the standard asymmetry ratio approaches zero at the spectral peak.

Before full analysis, each station was subjected to a q-stability check: a station was deemed reliable if $\max |h(q < 0)| < 3.0$. This threshold identifies the zero-crossing artefact that arises when the integrated profile of a detrended series oscillates near zero, causing the inverse-fluctuation weighting of negative q moments to diverge. All 16 stations in the final dataset passed this criterion; the excluded MOSC station did not. Because MF-DFA estimates scaling exponents from the statistics of detrended fluctuations, an abrupt, uncorrected level-shift introduces an artificial low-frequency component that inflates apparent persistence independently of genuine heliospheric signal. Retaining MOSC would therefore have biased both the station-level estimate for Moscow and, given the network-wide averaging used in Section 3.1.2, the reported network mean $\langle h(2)\rangle$. Its exclusion ensures that the reported network-level statistics reflect genuine heliospheric persistence rather than an instrumental artefact at a single station. All computations were performed using the Fathon Python library (version 1.3.3). All analysis notebooks, including the data preprocessing pipeline, MF-DFA and NTA computation scripts, surrogate test generator, and figure-reproduction code, are permanently archived in the public repository indicated in the Data Availability statement.

To determine the physical origin of the observed multifractality — whether it arises from long-range correlations in the time series or from the non-Gaussian shape of the amplitude distribution (broad PDF) — we applied a surrogate data test following Kantelhardt et al. [19]. For each of the 16 stations we generated $N = 1000$ surrogates of two types. Phase Randomization (PR) surrogates are obtained by randomising the Fourier phases of the preprocessed series while preserving their modulus; this destroys all temporal correlations while exactly preserving the marginal amplitude distribution. Amplitude Adjusted Fourier Transform (AAFT) surrogates additionally rescale the phase-randomized series back to the original rank-order values, thereby approximately preserving both the power spectrum and the amplitude distribution. For each surrogate we computed $\Delta\alpha$ using the same MF-DFA parameters as for the original series. If $\Delta\alpha_{\text{orig}}$ exceeds the surrogate distribution significantly ($p < 0.05$, one-sided), the corresponding source of multifractality is confirmed: rejection of the PR null hypothesis implies that long-range correlations contribute; additional rejection of the AAFT null hypothesis implies that nonlinear (beyond-Gaussian) correlations are also present.

To track the temporal evolution of multifractal parameters, we applied a sliding-window MF-DFA. A window of $W = 730$ days was advanced through each station's record in steps of one day, yielding a time series of $h(2)$ and $\Delta\alpha$ centred on the midpoint of each window. The window length of 730 days was chosen to match the quasi-biennial oscillation (QBO) window used by Varotsos [7] for their entropy analysis, thereby ensuring direct comparability between the two methodological frameworks. Within each window, segment sizes spanned 2^3 to 2^7 days (8–128 days), which satisfies the requirement that the maximum segment size not exceed one quarter of the window length. The same moment orders and polynomial order as in the static analysis were used. Results were cached to disk to facilitate reproducibility without recomputation.

The sensitivity of the results to the two main preprocessing choices was assessed as follows. Replacing the linear interpolation limit of 10 days with limits of 0 and 5 days produces maximum deviations in $h(2)$ of 1.06% (ATHN) and 0.43% (JUNG), confirming that gap-filling does not drive the scaling results (Table 2). Replacing the 365-day detrending window with 180-day and 730-day alternatives yields qualitatively identical rolling MF-DFA dynamics under all three choices: the solar-minimum decrease in $h(2)$ (ATHN: $\langle h(2)\rangle \approx 0.96$–$0.97$ in 2019–2020) and the elevated $h(2)$ at FD onset ($\langle h(2)\rangle \approx 1.07$–$1.10$) are present irrespective of the detrending window. These checks confirm that the identified patterns reflect a genuine heliospheric signal rather than preprocessing artefacts.

2.4 Natural Time Analysis

Natural Time Analysis (NTA) was introduced by Varotsos et al. [32] as a framework for studying the dynamics of complex systems by focusing on the order and energy content of events rather than

Table 2: Sensitivity of static MF-DFA parameters to gap-filling strategy for Athens (ATHN) and Jungfraujoch (JUNG). The reference choice used throughout the paper is a linear interpolation limit of 10 days. N_{valid}: number of non-missing days after preprocessing.

Station	**Gap limit (days)**	$h(2)$	$\Delta\alpha$	N_{valid}
ATHN	0	0.986	0.490	5532
ATHN	5	0.988	0.972	5715
ATHN	10	0.996	1.242	5744
JUNG	0	0.984	0.428	5767
JUNG	5	0.988	0.452	5796
JUNG	10	0.988	0.452	5796

on conventional clock time. In natural time each event k in a sequence of N events is assigned the normalised index $\chi_k = k/N$, and a probability weight

$$p_k = \frac{Q_k}{\sum_{n=1}^{N} Q_n}, \tag{4}$$

where Q_k is the energy (or intensity) of the k-th event.

Two key quantities are derived from this representation. The variance in natural time,

$$\kappa_1 = \langle\chi^2\rangle - \langle\chi\rangle^2 = \sum_{k=1}^{N} p_k \chi_k^2 - \left(\sum_{k=1}^{N} p_k \chi_k\right)^2, \tag{5}$$

is linked to criticality: for a wide class of dynamical systems approaching a critical transition, $\kappa_1 \to 0.070$ [32, 33]. We emphasise that "criticality" here is used in the operational, statistical sense defined within NTA theory — i.e., κ_1 approaching the empirically calibrated value 0.070 observed across a wide class of complex systems prior to abrupt transitions — and does not imply that we have established or claim to have established a physical phase transition in the heliospheric plasma in the thermodynamic sense. For a uniform distribution of event energies, $\kappa_1 = 1/12 \approx 0.0833$. The robustness of natural-time order parameter fluctuations and their predictive performance in complex systems have also been quantified using receiver operating characteristic analysis in previous work [34, 35].

The entropy in natural time is defined as

$$S = \langle\chi \ln \chi\rangle - \langle\chi\rangle \ln\langle\chi\rangle, \tag{6}$$

with the corresponding time-reversed entropy S_- obtained by reversing the order of the event sequence. The difference $\Delta S = S - S_-$ characterises the time irreversibility of the dynamics. For a uniform energy distribution, $S_u = (\ln 2)/2 - 1/4 \approx 0.0966$.

Following Varotsos [7], we applied a rolling NTA with the same 730-day window and one-day step as the rolling MF-DFA, computing κ_1 and S for each window. This simultaneous application of rolling NTA and rolling MF-DFA to the same data windows enables a direct empirical comparison of the two frameworks — a methodological step not previously attempted in the CR literature. All NTA computations were implemented in Python, with the formulation validated against the uniform-distribution analytical values ($\kappa_1 = 1/12$, $S = S_u$) as a sanity check.

3 Results

3.1 Static Multifractal Structure of the CR Network

3.1.1 Replication and validation: Athens and Jungfraujoch

We begin by applying static MF-DFA to the two stations analysed by Varotsos [7] — Athens (ATHN) and Jungfraujoch (JUNG) — over the full 2010–2025 period. Results are shown in Fig. 2.

For ATHN, we obtain $h(2) = 1.027$ and $\Delta\alpha = 1.296$. For JUNG we obtain $h(2) = 0.988$ and $\Delta\alpha = 0.452$. Both Hurst exponents are consistent with the scaling exponents $\alpha = 1.03$ and $\alpha = 1.07$ reported by Varotsos [7] for Athens and Jungfraujoch, respectively (derived from standard DFA2 rather than MF-DFA, which accounts for minor numerical differences). Values of $h(2) \approx 1$ confirm persistent $1/f$-type long-range correlations at both stations, consistent with long-range correlated dynamics in galactic CR modulation [7]. The generalized Hurst spectra $h(q)$ decrease monotonically with q for both stations. For ATHN, $h(q)$ ranges from $h(-5) = 1.91$ to $h(5) = 0.96$, a spread of ~ 0.95. For JUNG the range is narrower: $h(-5) = 1.13$ to $h(5) = 0.90$, a spread of ~ 0.23. This difference anticipates the larger spectral width of ATHN ($\Delta\alpha = 1.296$) relative to JUNG ($\Delta\alpha = 0.452$).

The considerably broader spectrum of ATHN reflects the higher geomagnetic cut-off rigidity of Athens ($R_c = 8.53$ GV vs $R_c = 4.49$ GV for JUNG): the Athens station detects only the harder, more energetically variable component of the primary CR spectrum, producing more heterogeneous intensity fluctuations and a wider singularity spectrum. Jungfraujoch, at high altitude (~3500 m) and intermediate rigidity, records a broader primary energy range with more uniform modulation, resulting in a narrower $f(\alpha)$ profile.

3.1.2 Network-scale characterisation: 16 stations

Table 3 and Fig. 3 summarise the static MF-DFA results for the full 16-station network.

All 16 stations yield $h(2) > 0.5$, confirming that persistent long-range correlations are universal across the global neutron monitor network, independent of geographic location, altitude, and geomagnetic cut-off rigidity. The Hurst exponents range from $h(2) = 0.753$ (BKSN, Baksan) to $h(2) = 1.202$ (JUNG1, Jungfraujoch NM64), with a network mean of $\langle h(2)\rangle = 1.00 \pm 0.09$. BKSN's lower value is consistent with its documented instrumental jumps [7]; excluding BKSN and JUNG1 as outliers gives $\langle h(2)\rangle = 1.01 \pm 0.05$, consistent with the $1/f$-type scaling found by Varotsos [7]. The anomalously high $h(2)$ at JUNG1 may also reflect the specific hardware configuration of the NM64-type detector, which differs from the older IGY-type counter at the same location (JUNG) and could respond differently to local atmospheric pressure corrections or count-rate normalisation. The unusually broad $\Delta\alpha$ at BKSN, beyond the instrumental jumps already noted, may additionally reflect its mid-latitude, moderate-altitude location, which is more exposed to localised atmospheric and geomagnetic disturbances than the polar or high-altitude stations in the network; disentangling instrumental from genuine environmental contributions at BKSN would require a station-specific diagnostic beyond the scope of this network-level study.

The spectral widths $\Delta\alpha$ range from 0.452 (JUNG) to 2.354 (BKSN), with $\langle\Delta\alpha\rangle = 1.35 \pm 0.53$. Low-rigidity polar stations (OULU, APTY, JUNG, JUNG1) tend to display narrower spectra ($\Delta\alpha \lesssim 0.6$), while mid-latitude stations with higher rigidities (BKSN, SOPO, NAIN, MXCO, FSMT) exhibit broader spectra ($\Delta\alpha \gtrsim 1.5$). This pattern is physically consistent with the rigidity-dependence of CR modulation: low-rigidity stations detect the softer, uniformly modulated component of the primary spectrum producing smoother, less multifractal fluctuations; high-rigidity stations detect only the harder, more intermittent component, yielding a richer scaling hierarchy.

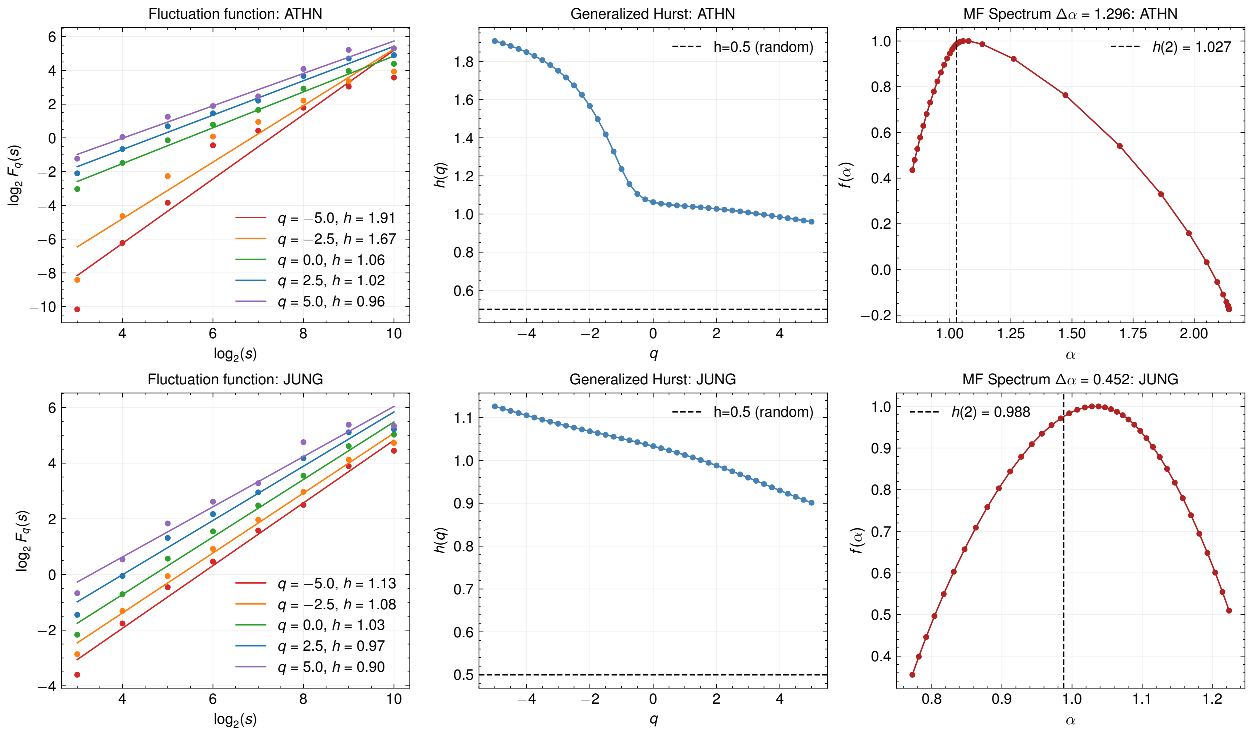

Figure 2: Static MF-DFA results for Athens (ATHN, top row) and Jungfraujoch IGY (JUNG, bottom row) over 2010–2025. Left: log–log plot of the q-th order fluctuation function $F_q(s)$ vs. segment size s for selected moment orders $q \in \{-5.0, -2.5, 0.0, +2.5, +5.0\}$. Centre: generalised Hurst spectrum $h(q)$. The monotonically decreasing dependence on q is the defining signature of multifractality; the dashed grey line marks $h = 0.5$. Right: multifractal singularity spectrum $f(\alpha)$. For ATHN: $h(2) = 1.027$, $\Delta\alpha = 1.296$. For JUNG: $h(2) = 0.988$, $\Delta\alpha = 0.452$.

3.1.3 Surrogate test: physical origin of multifractality

Table 4 and Fig. 4 report the results of the surrogate test applied to all 16 stations.

All 16 stations reject both the PR and AAFT null hypotheses at $p < 0.05$ (Table 4), confirming that nonlinear long-range correlations are the dominant source of multifractality across the global CR network. The excess of $\Delta\alpha_{\mathrm{orig}}$ over the PR surrogate mean ranges from +31% (JUNG) to +84% (SOPO), with a network mean of +73%. The AAFT test shows comparable excess values, indicating that the multifractality cannot be attributed to the linear power spectrum alone and genuinely reflects nonlinear temporal structure in the CR flux. Notably, Mexico City (MXCO) shows a larger $\Delta\alpha_{\mathrm{AAFT}} = 0.706$ than the other stations ($\Delta\alpha_{\mathrm{AAFT}} \approx 0.28$–$0.37$ for the rest), suggesting that the non-Gaussian character of its amplitude distribution contributes a non-negligible fraction of the observed multifractality — physically consistent with its high cut-off rigidity ($R_c = 8.28$ GV) and intermediate altitude, which produce a more intermittent detector response to hard CR primaries. The stations with the lowest z-scores (JUNG, JUNG1, OULU, APTY) are precisely the low-rigidity polar and high-altitude stations with the narrowest static spectra, where the multifractal signal above the surrogate baseline is weakest but still statistically unambiguous.

Table 3: Static MF-DFA results for the 16-station network (2010–2025). All stations pass the q-stability criterion ($\max |h(q < 0)| < 3.0$). Stations marked * were also analysed by Varotsos [7].

Code	**Station**	$h(2)$	$\Delta\alpha$	**Source**
AATB	Alma-Ata B	0.997	1.145	This work
APTY	Apatity	1.005	0.616	This work
ATHN*	Athens	1.027	1.296	Varotsos [7]/this work
BKSN	Baksan	0.753	2.354	This work
FSMT	Fort Smith	1.049	1.713	This work
INVK	Inuvik	0.984	1.566	This work
JUNG*	Jungfraujoch IGY	0.988	0.452	Varotsos [7]/this work
JUNG1	Jungfraujoch NM64	1.202	0.546	This work
KERG	Kerguelen	0.979	1.541	This work
MXCO	Mexico City	0.980	1.722	This work
NAIN	Nain	1.020	1.741	This work
NEWK	Newark	1.011	1.680	This work
OULU	Oulu	0.989	0.528	This work
PSNM	Doi Inthanon	0.967	0.978	This work
SOPO	South Pole	1.010	2.076	This work
THUL	Thule	1.005	1.622	This work
Network mean		1.00 ± 0.09	1.35 ± 0.53	

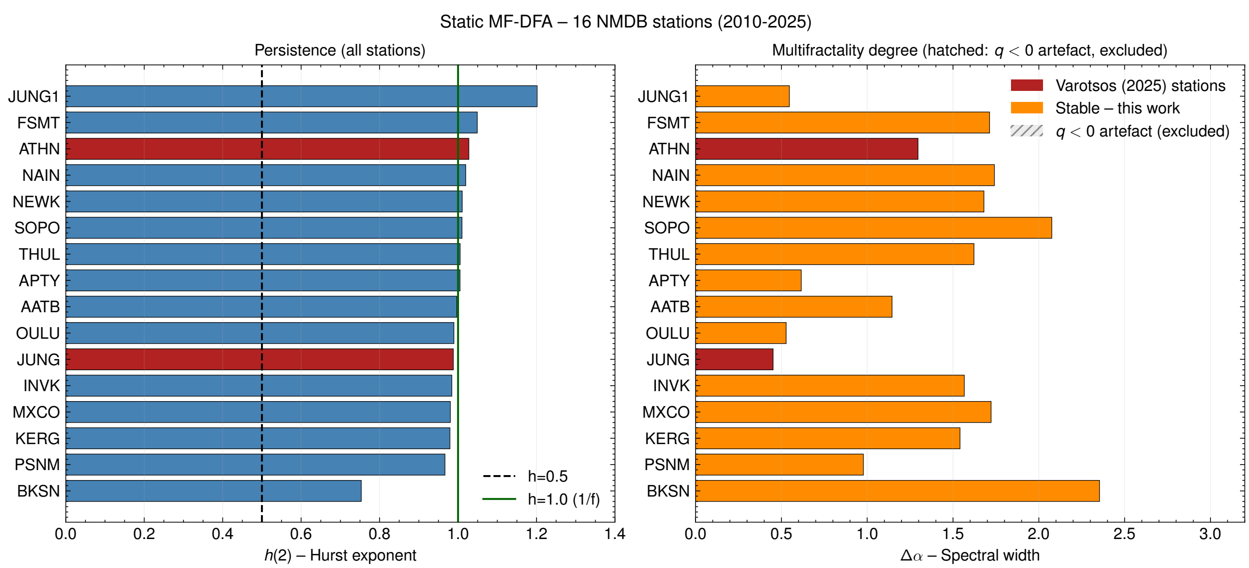

Figure 3: Summary of static MF-DFA parameters for the 16-station NMDB network (2010–2025). Left: generalised Hurst exponent $h(2)$ ranked in ascending order. Red bars: stations analysed by Varotsos [7]; blue bars: stations introduced in this work. All 16 stations satisfy $h(2) > 0.5$. Right: multifractal spectral width $\Delta\alpha$; network mean $\langle \Delta\alpha \rangle = 1.35 \pm 0.53$.

3.2 Dynamic Multifractal Evolution and Network-wide Coherence

3.2.1 Temporal evolution of multifractal parameters

The rolling MF-DFA (730-day window, 1-day step) reveals a non-stationary multifractal structure at both ATHN and JUNG (Figs. 5–6). At ATHN, $h(2)$ oscillates in the range ~ 0.7–1.2, with

Table 4: Surrogate test for the origin of multifractality (1000 surrogates per type per station). $\Delta\alpha_{\mathrm{orig}}$: observed spectral width. $\Delta\alpha_{\mathrm{PR}}$: mean spectral width of Phase Randomization surrogates (correlations destroyed, PDF preserved). $\Delta\alpha_{\mathrm{AAFT}}$: mean spectral width of AAFT surrogates (PDF and power spectrum preserved). z_{PR}: z-score of $\Delta\alpha_{\mathrm{orig}}$ relative to the PR surrogate distribution. p_{PR}, p_{AAFT}: one-sided p-values. All 16 stations reject both null hypotheses at $p < 0.05$, confirming that nonlinear long-range correlations are the dominant source of multifractality across the network.

Station	$\Delta\alpha_{\mathrm{orig}}$	$\Delta\alpha_{\mathrm{PR}}$	z_{PR}	$\Delta\alpha_{\mathrm{AAFT}}$	p_{PR}	p_{AAFT}
AATB	1.145	0.327	13.56	0.298	<0.001	<0.001
APTY	0.616	0.326	4.80	0.259	<0.001	<0.001
ATHN	1.296	0.291	15.76	0.335	<0.001	<0.001
BKSN	2.354	0.451	35.23	0.840	<0.001	<0.001
FSMT	1.713	0.312	20.77	0.273	<0.001	<0.001
INVK	1.566	0.332	20.29	0.332	<0.001	<0.001
JUNG	0.452	0.309	2.36	0.312	0.020	0.017
JUNG1	0.546	0.339	3.52	0.230	0.002	<0.001
KERG	1.541	0.306	20.90	0.314	<0.001	<0.001
MXCO	1.722	0.306	24.55	0.706	<0.001	<0.001
NAIN	1.741	0.316	23.35	0.281	<0.001	<0.001
NEWK	1.680	0.309	21.22	0.293	<0.001	<0.001
OULU	0.528	0.316	3.57	0.313	0.002	0.001
PSNM	0.978	0.329	10.55	0.363	<0.001	<0.001
SOPO	2.076	0.328	27.99	0.308	<0.001	<0.001
THUL	1.622	0.330	20.61	0.294	<0.001	<0.001

elevated $\Delta\alpha \gtrsim 2.0$ concentrated around 2015–2017. At JUNG, $h(2)$ varies between ~ 0.5 and 1.2 with a lower $\Delta\alpha$ baseline, consistent with its narrower static spectrum.

A feature common to both stations is a decrease in $h(2)$ during 2019–2020, coinciding with the solar minimum between cycles 24 and 25. During this period CRI is high and smoothly varying; the reduced intermittency produces lower effective persistence in the detrended anomaly series. Conversely, the rising phase of solar cycle 25 (2023–2025) shows elevated $h(2)$ at both stations, consistent with stronger and more structured heliospheric modulation.

3.2.2 Network-wide coherent dynamics

The network-wide heatmaps (Fig. 7) reveal coherent spatiotemporal structures in both $h(2)$ and $\Delta\alpha$.

Two dominant structures appear in the $h(2)$ heatmap. First, a network-wide decrease around 2015–2016 affects all latitudes and rigidities simultaneously, corresponding to the declining phase of solar cycle 24. Second, the 2019–2020 solar minimum produces a second coherent decrease, particularly pronounced at mid-latitude stations (ATHN, APTY, OULU, KERG). The two 2024 Forbush events produce a spatially coherent response with elevated $h(2)$ values at multiple stations, confirming that these are global heliospheric modulations rather than local artefacts.

The $\Delta\alpha$ heatmap shows elevated values ($\gtrsim 2.5$) at several stations (ATHN, FSMT, KERG, JUNG) during 2015–2017, consistent with enriched multifractal structure during a period of sustained moderate solar activity.

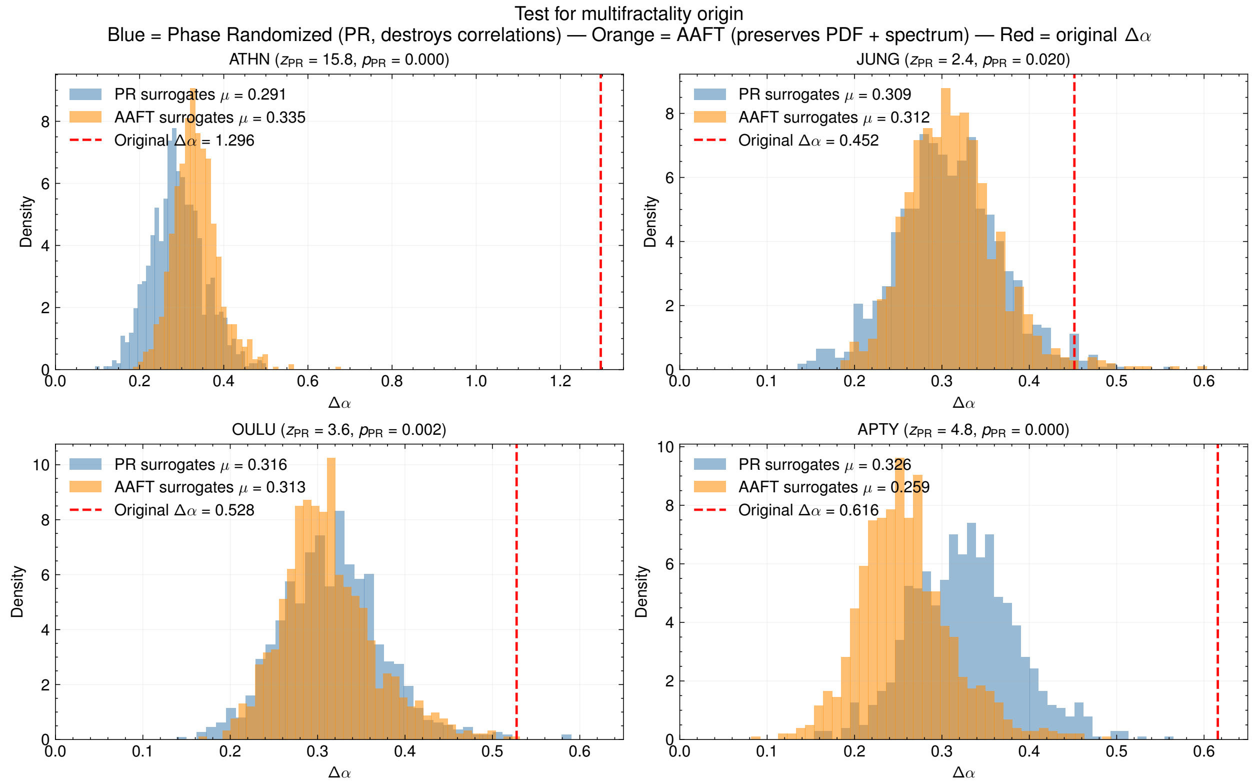

Figure 4: Surrogate test for multifractality origin at four representative stations (ATHN, JUNG, OULU, APTY). Blue histograms: $\Delta\alpha$ distribution from 1000 Phase Randomization (PR) surrogates, which destroy all temporal correlations while preserving the amplitude distribution. Orange histograms: $\Delta\alpha$ from 1000 AAFT surrogates, which additionally preserve the power spectrum. Red vertical line: $\Delta\alpha$ of the original series. At all four stations, $\Delta\alpha_{\text{orig}}$ lies far above both surrogate distributions, confirming that nonlinear long-range correlations — not the shape of the amplitude distribution — are the dominant source of multifractality. The z-scores range from 2.4 (JUNG) to 15.8 (ATHN).

3.2.3 Spectral width behavior around the 2024 Forbush Decreases

Fig. 8 shows the temporal evolution of $\Delta\alpha$ in the 180 days before and 60 days after each 2024 Forbush decrease event, for ATHN and JUNG. We note that the analysis in this section is descriptive and based on two events only; the statistical generality of the $\Delta\alpha$ signal across the broader FD catalogue is examined in Section 3.4.

For JUNG, $\Delta\alpha$ undergoes a systematic decrease beginning ∼120 days before the 24 March 2024 onset (reaching ∼27% below baseline at the event) and ∼150 days before the 10 May 2024 onset (∼20% reduction). The difference between JUNG and ATHN is physically coherent: JUNG's lower cut-off rigidity ($R_c = 4.49$ GV vs 8.53 GV) makes it sensitive to a softer component of the primary CR spectrum that is more responsive to the early restructuring of the heliospheric magnetic field as an ICME propagates outward. As this restructuring imposes a single dominant modulation scale, the multifractal hierarchy narrows and $\Delta\alpha$ decreases. This mechanistic account remains a plausible interpretation rather than a confirmed mechanism: it is consistent with the rigidity contrast between the two stations, but direct validation would require independent measurements of heliospheric magnetic field structure together with a larger event catalogue and higher temporal

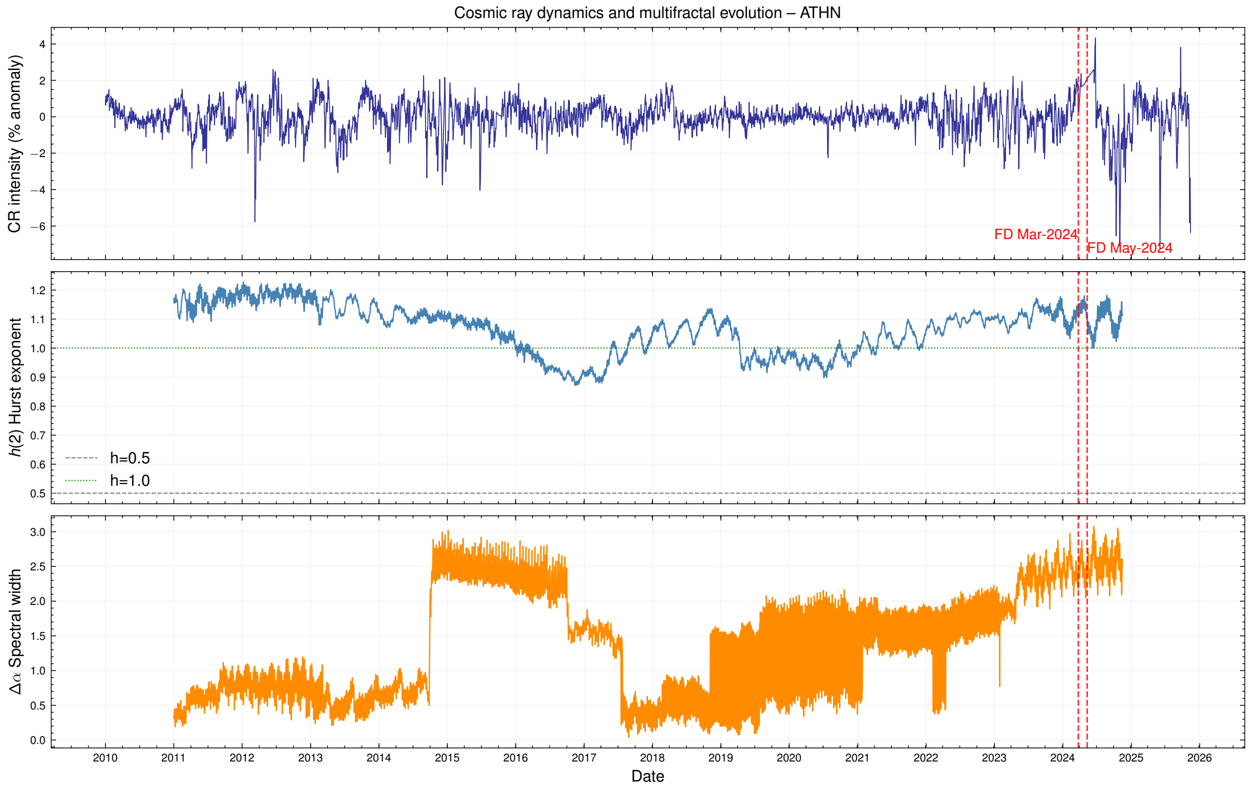

Figure 5: Rolling MF-DFA for Athens (ATHN), 730-day sliding window, 2010–2025. Top: preprocessed CR anomaly (%). Middle: $h(2)$ (horizontal lines at $h = 0.5$ and $h = 1.0$). Bottom: $\Delta\alpha$. Red dashed lines mark the 24 March and 10 May 2024 Forbush decrease onsets. The 2019–2020 solar minimum is visible as a network-wide decrease in $h(2)$.

resolution data. Whether this behaviour is statistically robust across a broader FD catalogue is examined next.

3.3 Empirical Connection between MF-DFA and Natural Time Analysis

3.3.1 Joint rolling evolution

Fig. 9 shows the simultaneous rolling evolution of $h(2)$, κ_1, and S for ATHN over 2010–2025. During 2019–2020 (solar minimum), $h(2)$ is at a local minimum while κ_1 and S are elevated — consistent with a more random, uniform-energy CR flux. During periods of heightened solar activity (2013–2014 and 2023–2024), $h(2)$ is elevated and κ_1 is reduced, indicating stronger long-range ordering. Near the 2024 Forbush events, the two frameworks evolve coherently: $h(2)$ increases, κ_1 approaches (but does not reach at daily resolution) $\kappa_{1,\text{crit}} = 0.070$, and S drops below S_u. This joint co-evolution, detected independently by MF-DFA and NTA, motivates a systematic multi-event analysis (Section 3.4).

3.3.2 Scatter analysis: quantifying the NTA–MF-DFA relationship

Fig. 10 shows the scatter of κ_1 against $h(2)$ and $\Delta\alpha$ for all 730-day rolling windows of the ATHN record. The correlation between κ_1 and $h(2)$ is statistically significant but modest (Pearson $r = 0.117$, $p < 10^{-16}$; Spearman $\rho = 0.117$), and weaker still for κ_1 vs $\Delta\alpha$ ($r = 0.043$, $p = 2.3 \times 10^{-3}$).

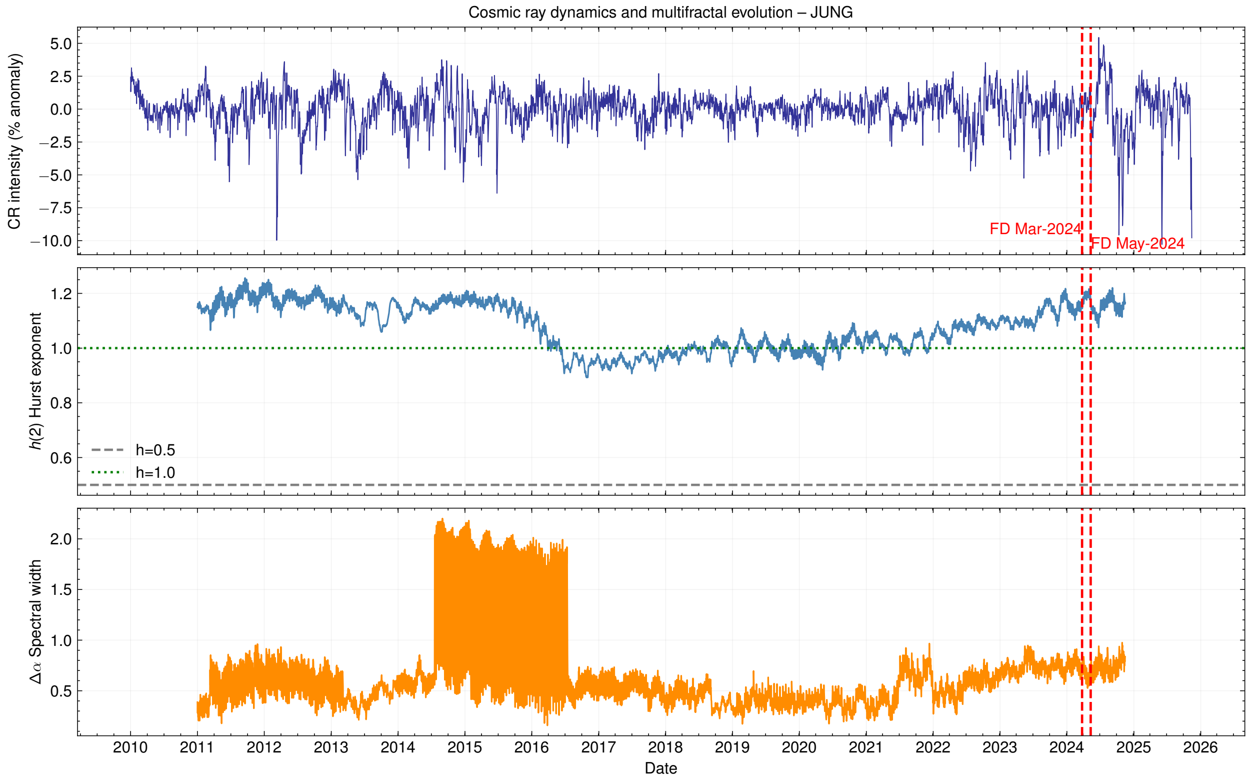

Figure 6: Same as Fig. 5 for Jungfraujoch IGY (JUNG). The baseline $\Delta\alpha$ is consistently lower than at ATHN, consistent with the narrower static spectrum ($\Delta\alpha = 0.452$ vs 1.296).

The $r^2 \approx 1.4\%$ shared variance quantifies the degree of complementarity: MF-DFA characterises the scaling hierarchy of fluctuation amplitudes across temporal scales, while NTA characterises the order and energy weighting of the event sequence. Each framework carries predominantly independent information about the CR dynamics.

3.4 Multi-event Analysis: Systematic Signatures at Forbush Decrease Conditions

To assess the generality of the joint MF-DFA–NTA behaviour observed around the 2024 events, we extend the analysis to all nine major Forbush decreases (magnitude $> 6\%$) recorded within our study period (Table 5).

3.4.1 Full time series with FD markers

Fig. 11 overlays all nine FD events on the rolling $h(2)$, κ_1, and S time series for ATHN, with colours encoding event magnitude.

Visual inspection of Fig. 11 suggests that most major FD events coincide with periods of elevated $h(2)$ and depressed κ_1 relative to the broader time series. The 2019–2020 solar minimum, during which no large FDs occurred, is the most prominent counter-example: both $h(2)$ and κ_1 show their most extreme excursions in the opposite direction.

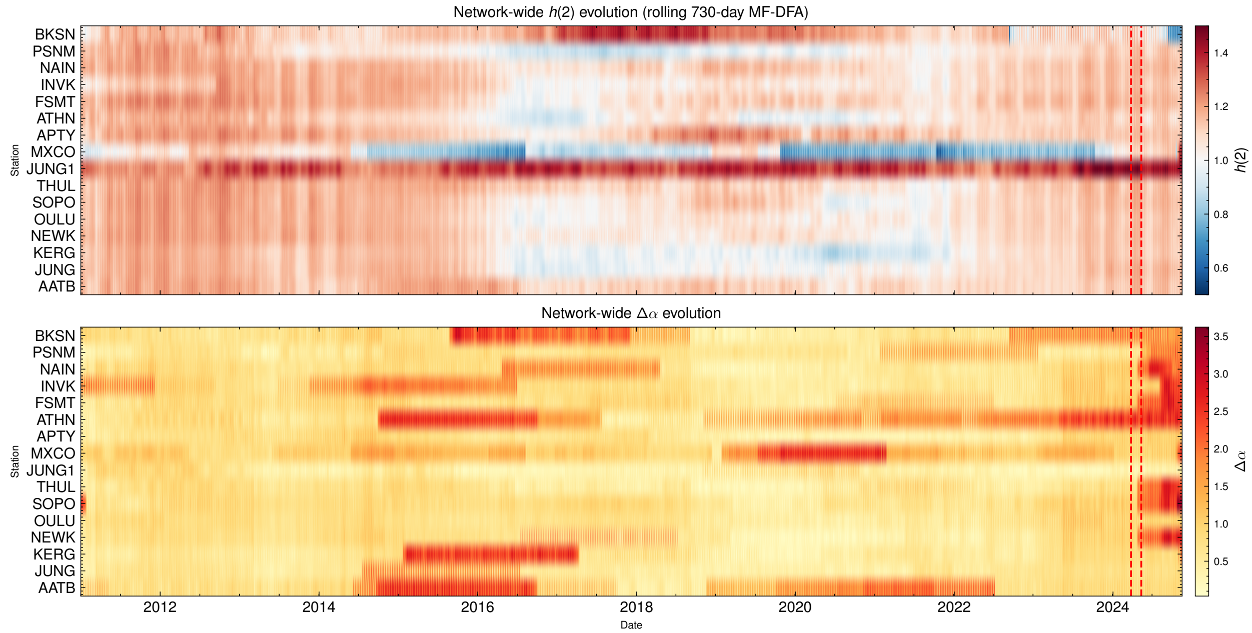

Figure 7: Network-wide evolution of $h(2)$ (top) and $\Delta\alpha$ (bottom) for all 16 NMDB stations, 2012–2025 (rolling 730-day MF-DFA). Cool colours indicate lower persistence; warm colours indicate higher persistence. The 2015–2016 and 2019–2020 decreases in $h(2)$ are coherent across latitudes and rigidities. Red dashed lines mark the 2024 Forbush decrease onsets. Station acronyms are defined in Table 1.

Table 5: Forbush decrease events used in the multi-event analysis (NMDB catalogue, magnitude $> 6\%$, 2010–2025).

Date	Magnitude (%)	Solar cycle
2011-10-24	6.01	24 (rising)
2012-03-08	10.40	24 (maximum)
2012-07-14	6.70	24 (maximum)
2015-06-22	8.57	24 (declining)
2017-09-07	6.41	24 (declining)
2021-11-03	9.68	25 (rising)
2023-04-23	6.57	25 (rising)
2024-03-24	11.47	25 (maximum)
2024-05-10	15.32	25 (maximum)

3.4.2 Superposed epoch analysis

Fig. 12 shows the superposed epoch analysis (SEA), stacking the rolling $h(2)$, κ_1, and $\Delta\alpha$ time series in a $\pm$365-day window centred on each FD onset. Six of the nine events yield sufficient data on both sides of the window (the three earliest events fall too close to the rolling start to contribute a full -365-day interval) and are included in the stack.

The SEA reveals a consistent structure in the median curves. At both ATHN and JUNG, the median $h(2)$ is elevated above its long-term background level in a broad region around the FD onset, rising in the $\sim$200 days preceding the event and recovering in the $\sim$100 days following it. The median κ_1 at ATHN is depressed below background near lag$=0$, approaching its minimum

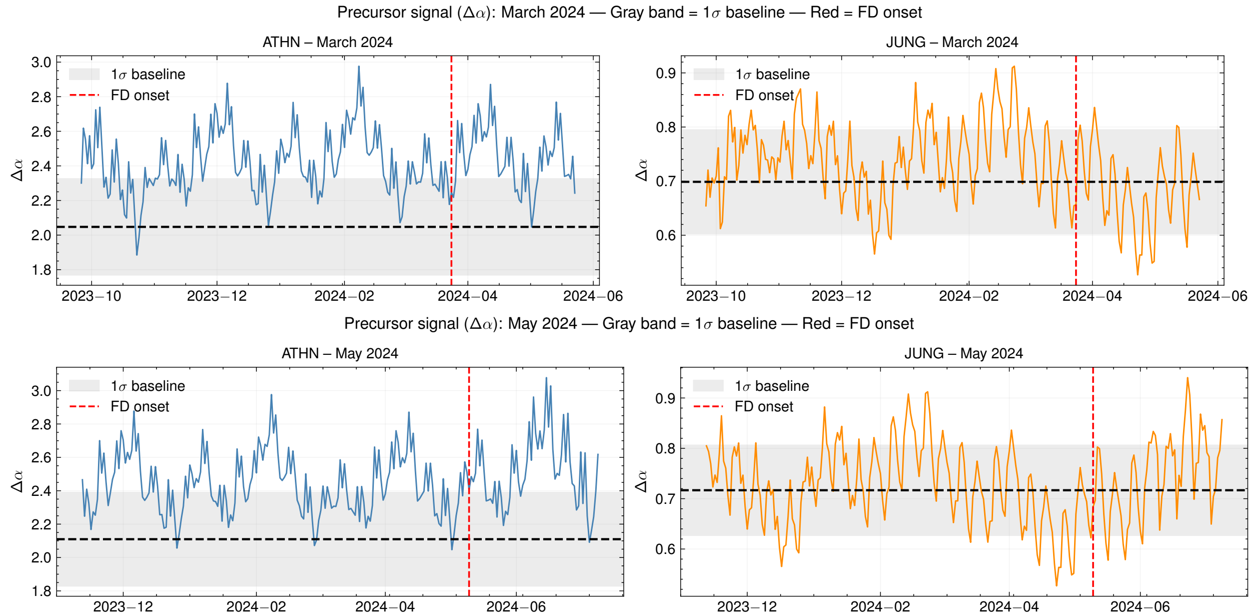

Figure 8: Temporal evolution of $\Delta\alpha$ in the 180 days preceding and 60 days following the two major 2024 Forbush decreases. Left panels: Athens (ATHN, $R_c = 8.53$ GV). Right panels: Jungfraujoch IGY (JUNG, $R_c = 4.49$ GV). Grey band: $\pm 1\sigma$ baseline over the preceding 365 days. Red dashed line: FD onset. At JUNG, $\Delta\alpha$ decreases $\sim$120 days before the March event ($\sim$27% below baseline) and $\sim$150 days before the May event ($\sim$20% below baseline). No equivalent behaviour is detectable at ATHN. (upper) March 2024 Forbush decrease (onset: 24 March 2024). (bottom) May 2024 Forbush decrease (onset: 10 May 2024).

close to the FD onset and recovering thereafter. These features are present in most individual events (thin lines), indicating that the pattern is not driven by one or two extreme episodes.

3.4.3 Pattern check and statistical tests

Table 6 reports the MF-DFA and NTA parameter values at each FD onset, evaluated from the 730-day rolling series. The background reference level is computed from all windows not within 90 days of any catalogued FD event (3670 windows; $h(2)_{\text{bg}} = 1.053$, $\kappa_{1,\text{bg}} = 0.082$).

Seven of nine events (78%) show $h(2)$ above the background mean at FD onset; an equal fraction show κ_1 below background. One-sided Mann–Whitney U tests confirm that $h(2)$ values at FD onset are statistically higher than the background distribution ($U = 22754$, $p = 0.025$) and that κ_1 values are statistically lower ($U = 10989$, $p = 0.041$). We note that the rolling windows used to construct the background distribution are not statistically independent due to overlap; the resulting p-values should therefore be interpreted as descriptive measures of distributional separation rather than strict hypothesis tests under independence assumptions. Both results are significant at the 5% level. The corresponding rank-biserial effect sizes are $r = -0.378$ for $h(2)$ and $r = -0.335$ for κ_1, both classified as *medium* by standard benchmarks ($|r| \in [0.3, 0.5]$). The medium effect size suggests that the regime signal is systematic but not deterministic: it reflects a probabilistic modulation of FD occurrence rather than a triggering mechanism. In practical terms, elevated $h(2)$ and depressed κ_1 increase the likelihood of encountering large FD conditions but do not guarantee their occurrence. The binomial test for 7/9 is marginally non-significant ($p = 0.090$), reflecting the low statistical power of binomial counting tests at $N = 9$; the Mann–Whitney results, which exploit

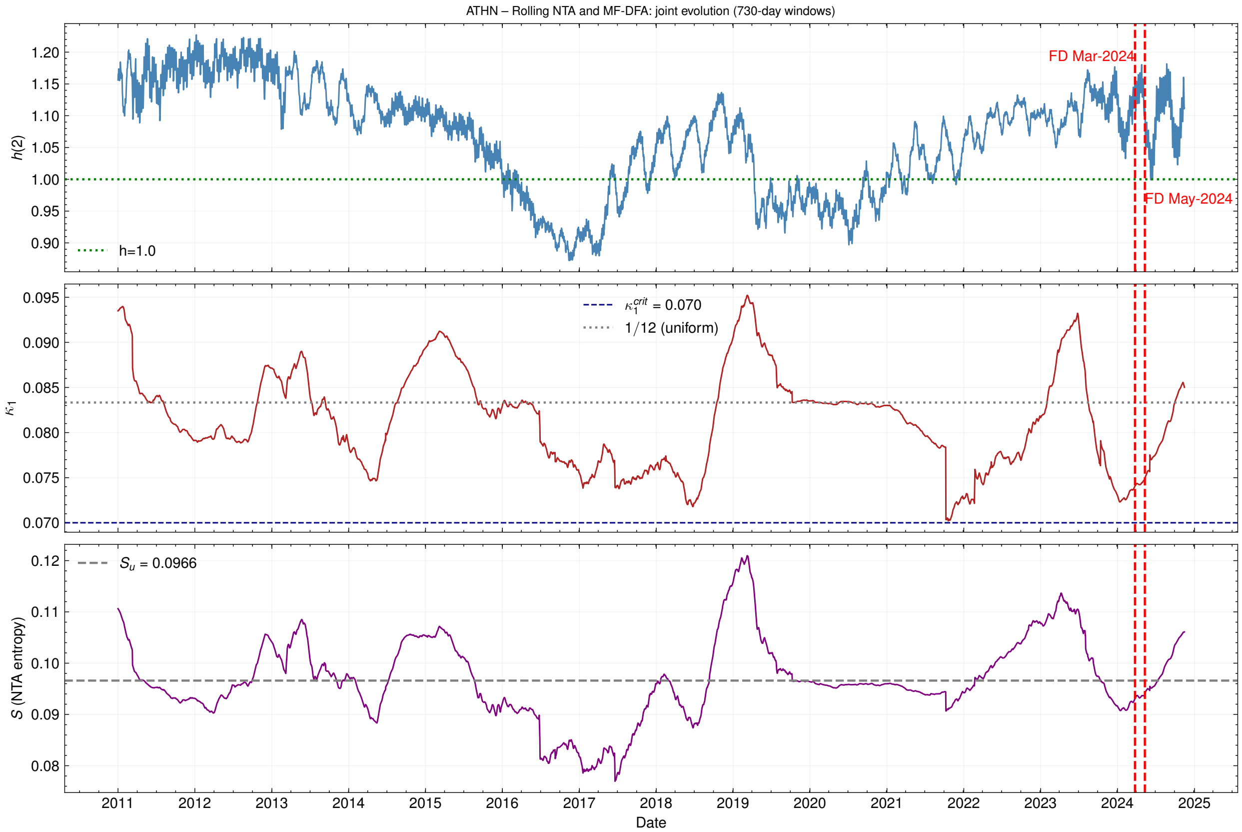

Figure 9: Joint rolling evolution (730-day window) of $h(2)$ (top), κ_1 (middle), and NTA entropy S (bottom) for ATHN. Middle: $\kappa_{1,\mathrm{crit}} = 0.070$ (blue dashed) and 1/12 (grey dotted). Bottom: $S_u = 0.0966$ (grey dashed). Red dashed lines mark the 24 March and 10 May 2024 FD onsets. Near the 2024 events, $h(2)$ increases toward ∼1.15–1.20 while κ_1 decreases toward ∼0.073 and S drops below S_u, all consistent with a system approaching a critical transition.

the full background distribution rather than a binary count, are the more informative statistic here.

Table 6: MF-DFA and NTA parameter values at each FD onset (ATHN). $h(2)_{\mathrm{FD}}$: Hurst exponent at FD date. $\kappa_{1,\mathrm{FD}}$: NTA variance at FD date. Comparison columns indicate deviation from background mean ($h(2)_{\mathrm{bg}} = 1.053$, $\kappa_{1,\mathrm{bg}} = 0.082$). ↑ = above background; ↓ = below background.

Date	**Mag.**	$h(2)$	$h(2) \gtrless h(2)_{\mathrm{bg}}$	κ_1	$\kappa_1 \gtrless \kappa_{1,\mathrm{bg}}$
2011-10-24	6.0%	1.155	↑	0.080	↓
2012-03-08	10.4%	1.153	↑	0.080	↓
2012-07-14	6.7%	1.171	↑	0.079	↓
2015-06-22	8.6%	1.070	↑	0.088	↑
2017-09-07	6.4%	1.049	↓	0.075	↓
2021-11-03	9.7%	1.040	↓	0.071	↓
2023-04-23	6.6%	1.088	↑	0.091	↑
2024-03-24	11.5%	1.153	↑	0.074	↓
2024-05-10	15.3%	1.108	↑	0.075	↓
Count: $h(2) \gtrless h(2)_{\mathrm{bg}}$		7/9 events above background			
Count: $\kappa_1 \gtrless \kappa_{1,\mathrm{bg}}$		7/9 events below background			

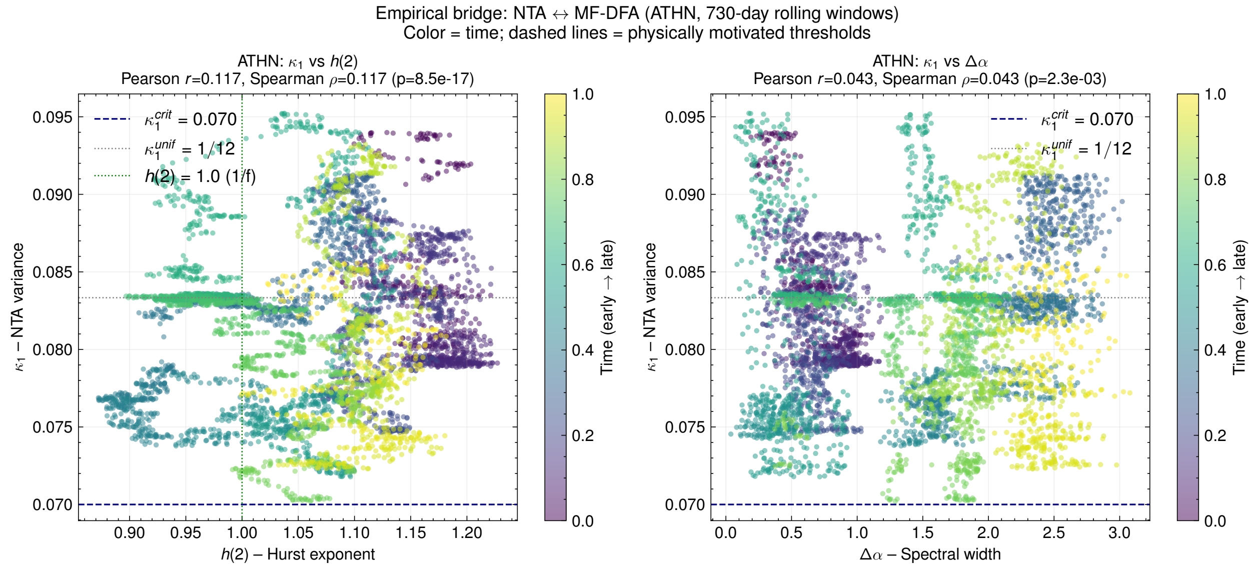

Figure 10: Scatter of κ_1 against $h(2)$ (left) and $\Delta\alpha$ (right) for all 730-day rolling windows (ATHN, 2012–2025). Colour encodes time (purple = early, yellow = recent). Dashed blue: $\kappa_1 = 0.070$ [32]; dotted grey: $\kappa_{\text{unif}} = 1/12$; dotted green: $h(2) = 1.0$. Pearson $r = 0.117$, Spearman $\rho = 0.117$ ($p < 10^{-16}$) for κ_1 vs $h(2)$; $r = 0.043$ ($p = 2.3 \times 10^{-3}$) for κ_1 vs $\Delta\alpha$. The colour gradient reveals secular solar-cycle evolution rather than random scatter. The modest shared variance ($r^2 \approx 1.4\%$) confirms complementarity rather than redundancy of the two frameworks.

To verify that any single event in the catalogue does not drive the result, we performed a bootstrap analysis resampling the nine FD parameter values with replacement (10 000 iterations) and re-running the Mann–Whitney test against the full background distribution at each iteration (Fig. 13). For $h(2)$, 66% of bootstrap resamples yield $p < 0.05$ (median $p = 0.025$); for κ_1, 56% yield $p < 0.05$ (median $p = 0.039$). The result is therefore not dominated by a single influential event and is moderately robust to the specific composition of the nine-event catalogue.

To address the non-independence of overlapping rolling windows, we estimated the effective background sample size using the integrated autocorrelation time of the background $h(2)$ series. The lag-1 autocorrelation is $\rho_1 = 0.995$ and the first zero-crossing occurs at lag 499 days, yielding an integrated autocorrelation time $\tau_{\text{int}} \approx 519$ days — comparable to the 730-day window length itself, as expected for a heavily overlapping sliding-window statistic. The effective number of statistically independent background observations is therefore $n_{\text{eff}} = n/\tau_{\text{int}} \approx 7$, far smaller than the nominal $n = 3670$. As a conservative robustness check, we repeated the Mann–Whitney tests using only background windows spaced at least 730 days apart (seven genuinely independent observations). For κ_1, the result remains statistically significant under this conservative test ($p = 0.027$), confirming the robustness of the natural-time variance signal to the window-overlap structure. For $h(2)$, the significance is not preserved ($p = 0.34$), reflecting the loss of statistical power when the effective background sample reduces to $n_{\text{eff}} \approx 7$. We therefore consider the κ_1 result as the more statistically robust of the two, while the $h(2)$ result, though directionally consistent and supported by the joint-state and superposed epoch analyses, should be interpreted with appropriate caution.

The $\Delta\alpha$ signal observed at JUNG for the two 2024 events (Section 3.3) does not reach statistical significance across the full nine-event catalogue ($p = 0.998$ for the one-sided Mann–Whitney test of $\Delta\alpha <$ background at JUNG), confirming that the $\Delta\alpha$ decrease is characteristic of the most extreme events and/or of the specific heliospheric conditions of solar cycle 25 maximum rather than

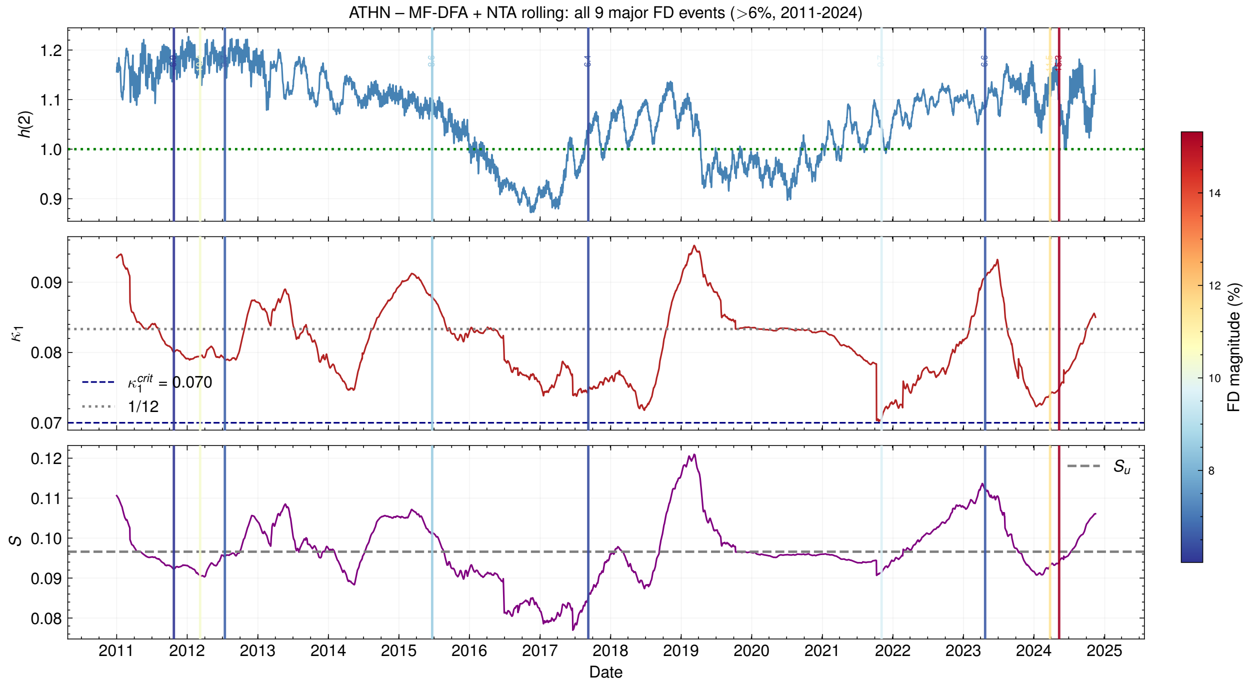

Figure 11: Rolling MF-DFA and NTA parameters for ATHN (2012–2025) with all nine major FD events marked (coloured vertical lines, colour = FD magnitude). Top: $h(2)$. Middle: κ_1 with $\kappa_{1,\mathrm{crit}} = 0.070$ (blue dashed) and 1/12 (grey dotted). Bottom: NTA entropy S with $S_u = 0.0966$ (grey dashed). Percentages indicate the FD magnitude at each event. Visual inspection suggests that most events coincide with elevated $h(2)$ and/or depressed κ_1, motivating the quantitative tests in Section 3.4.3.

a universal FD signature. This constitutes an example of an apparent precursor signal that does not generalise: the two individual cases are physically interpretable and motivate further investigation at higher temporal resolution and with a larger event catalogue, but cannot be elevated to a general predictive rule on the basis of the evidence available here.

Fig. 14 shows the scatter of the parameter values at each FD onset against the event magnitude.

The scatter plots reveal no significant correlation between event magnitude and either $h(2)$ ($r = 0.049$, $p = 0.90$) or κ_1 ($r = -0.418$, $p = 0.26$), though the latter shows a weak negative trend. This result is physically meaningful: the multifractal and NTA parameters characterise the state of the heliospheric CR modulation system over the preceding 730-day window, which is set by long-term solar activity conditions rather than by the instantaneous amplitude of a single ICME-driven event. The absence of a magnitude correlation confirms that the $h(2)$–κ_1 pattern is a signature of the heliospheric regime conducive to large FDs rather than a quantitative precursor of their amplitude.

3.5 Interpretation: a heliospheric regime signature

3.5.1 General remarks

The results of Sections 3.2–3.4 provide evidence for the following coherent picture, which is compatible with the earlier findings by Varotsos et al. [33]. During epochs of sustained solar activity that produce large Forbush decreases, the CR system enters a statistical regime signature characterised

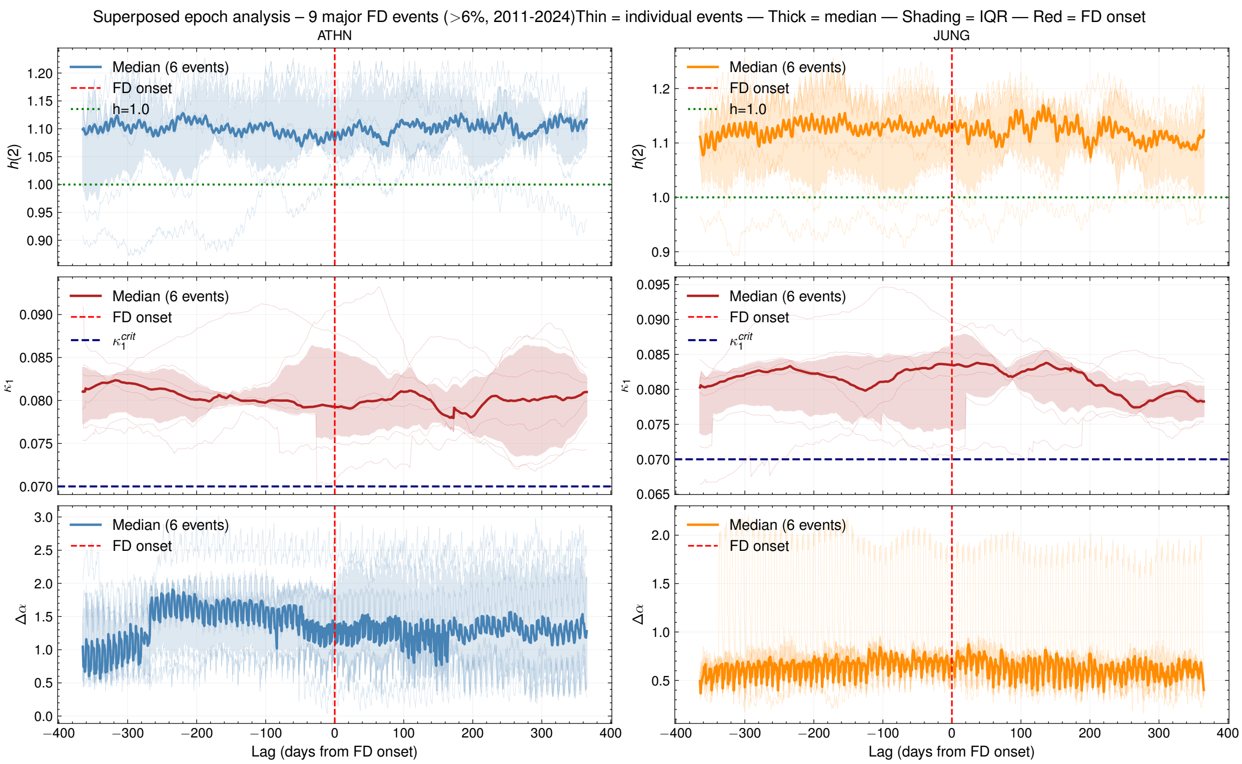

Figure 12: Superposed epoch analysis (SEA) centered on FD onset (lag= 0, red dashed), stacking six events that provide a full ±365-day window. Each thin line is one event; thick line is the median; shading is the inter-quartile range. Left column: Athens (ATHN). Right column: Jungfraujoch (JUNG). Rows show $h(2)$ (top), κ_1 (middle, ATHN only), and $\Delta\alpha$ (bottom). The median $h(2)$ is systematically above the long-term mean at lag= 0 at both stations. The median κ_1 is depressed around FD onset and recovers thereafter.

by:

- **Higher long-range persistence** ($h(2) > 1.05$): the heliospheric modulation becomes more correlated and structured over multi-month timescales, reflecting the complex superposition of ICME-driven disturbances, co-rotating interaction regions, and enhanced turbulence in the heliospheric magnetic field.
- **Lower NTA variance** ($\kappa_1 < 0.082$): the CR event sequence becomes more energetically organised in natural time, with the energy released in successive events distributed less uniformly than during quiet periods.
- **Anticorrelated solar minimum behaviour**: both signatures are reversed during the 2019–2020 solar minimum, where $h(2)$ reaches its lowest observed values and κ_1 rises toward 1/12 (the uniform-distribution reference), confirming that the pattern is physically driven by heliospheric activity rather than by data processing artefacts.

Competing physical mechanisms — including heliospheric turbulence, long-memory stochastic processes, and self-organised criticality — are not distinguished by the present analysis, as they may exhibit similar scaling behaviour. The surrogate test (Section 3.1.3) rules out a purely distributional origin but does not discriminate between correlation-based mechanisms.

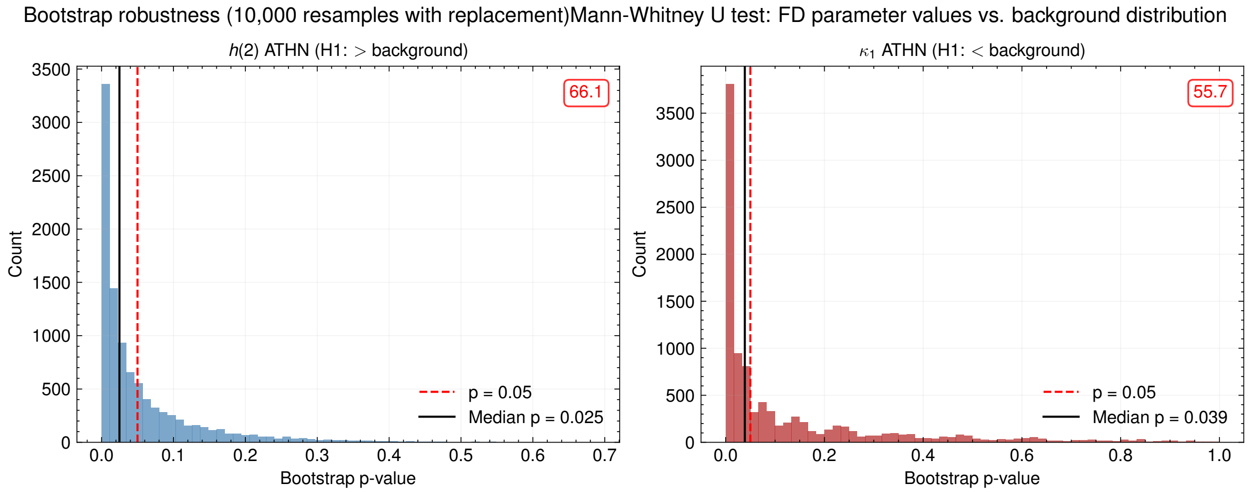

Figure 13: Bootstrap robustness of the Mann–Whitney tests (10 000 resamples with replacement from the nine FD events). Each histogram shows the distribution of p-values obtained by re-running the one-sided Mann–Whitney U test against the full background distribution at each bootstrap iteration. Left: $h(2)$ at ATHN (H_1: FD values $>$ background). Right: κ_1 at ATHN (H_1: FD values $<$ background). Red dashed line: $p = 0.05$. Black solid line: median p-value. The percentage of resamples yielding $p < 0.05$ (66% and 56% respectively) confirms that the statistical result is not driven by any single event.

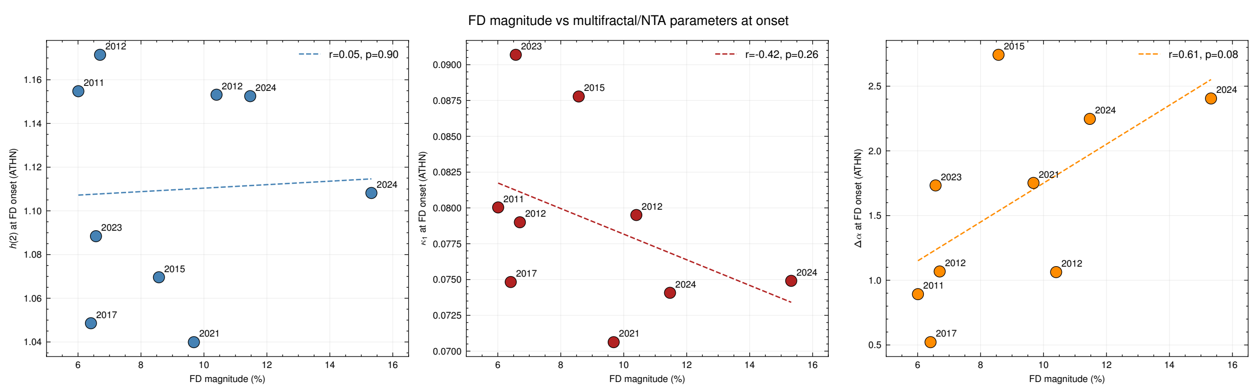

Figure 14: Parameter values at FD onset versus event magnitude for all nine events. Left: $h(2)$ at ATHN. Centre: κ_1 at ATHN. Right: $\Delta\alpha$ at ATHN. Dashed lines show linear regression; r and p values are reported for each panel. Neither $h(2)$ nor κ_1 shows a significant correlation with magnitude ($p > 0.05$), indicating that the elevated $h(2)$ / depressed κ_1 state is a qualitative condition associated with large FDs in general rather than a quantitative predictor of FD magnitude.

This regime is detected simultaneously and independently by MF-DFA and NTA — two frameworks that share only $r^2 \approx 1.4\%$ of their variance (Section 3.3) — providing mutual validation of the result. The joint application of the two frameworks therefore provides a more complete characterisation of the heliospheric state than either alone, confirming the complementarity argument advanced in Section 3.3 with empirical evidence spanning two solar cycles.

3.5.2 Joint-state analysis: FD occurrence rates across dynamical regimes

To quantify the relationship between the joint MF-DFA–NTA state and FD occurrence more directly, we partitioned the 5067 rolling windows into four dynamical regimes using the background thresholds $h(2)_{\mathrm{bg}} = 1.053$ and $\kappa_{1,\mathrm{bg}} = 0.082$ as boundaries (Table 7, Fig. 15).

The Q1 regime — characterised by simultaneously elevated $h(2)$ and depressed κ_1 — shows the highest FD occurrence rate (2.94 events per 1000 windows), approximately twice that of Q2 (1.39), which shares the same elevated $h(2)$ but disordered κ_1. This result demonstrates that neither metric alone is sufficient: the joint condition $h(2) > h(2)_{\mathrm{bg}}$ *and* $\kappa_1 < \kappa_{1,\mathrm{bg}}$ defines a more discriminating dynamical regime than either threshold applied independently.

Most strikingly, Q4 — the solar minimum state with simultaneously low $h(2)$ and high κ_1 — records *zero* large FD events across 1017 windows spanning the 2019–2020 solar minimum. This complete absence, in contrast to the 2.94/1000 rate of Q1, constitutes the sharpest empirical contrast in the dataset and confirms that the heliospheric regime, as characterised jointly by MF-DFA and NTA, is a meaningful discriminator of the conditions under which large transient CR modulation events occur.

A sensitivity analysis varying both thresholds by $\pm 5\%$ confirms that Q1 consistently shows the highest FD occurrence rate and Q4 consistently records zero events within this range, supporting the qualitative robustness of the four-regime partition. Beyond $\pm 10\%$ perturbation, the regime partitions become very small ($n_{\mathrm{FD}} \leq 1$ per quadrant) and the rate ordering becomes unreliable due to small-number statistics; conclusions drawn at those extreme threshold values should therefore be disregarded.

Table 7: Joint-state analysis: distribution of rolling windows and FD events across four dynamical regimes (ATHN, 2012–2025). Thresholds: $h(2)_{\mathrm{bg}} = 1.053$, $\kappa_{1,\mathrm{bg}} = 0.082$. FD rate is expressed as events per 1000 windows.

Regime	Condition	Windows	FD count	Rate (per 1000)
Q1 – Active organised	$h(2) > h(2)_{\mathrm{bg}}$, $\kappa_1 < \kappa_{1,\mathrm{bg}}$	1702	5	2.938
Q2 – Active disordered	$h(2) > h(2)_{\mathrm{bg}}$, $\kappa_1 \geq \kappa_{1,\mathrm{bg}}$	1435	2	1.394
Q3 – Quiet organised	$h(2) < h(2)_{\mathrm{bg}}$, $\kappa_1 < \kappa_{1,\mathrm{bg}}$	913	2	2.191
Q4 – Solar minimum	$h(2) < h(2)_{\mathrm{bg}}$, $\kappa_1 \geq \kappa_{1,\mathrm{bg}}$	1017	0	0.000

4 Discussion

4.1 Physical interpretation of the heliospheric regime signature

The central empirical finding of this paper — that large Forbush decreases are systematically associated with elevated CR persistence $h(2)$ and reduced NTA variance κ_1 in 730-day rolling windows — invites a physical interpretation in terms of heliospheric plasma dynamics. We stress that the 730-day window reflects a long-term conditioning of the heliospheric state rather than a short-term precursor: the signal does not arise from transient changes occurring immediately before the FD onset, but from the multi-month accumulation of structured solar activity that makes the heliosphere conducive to producing large transient modulation events.

During periods of sustained solar activity — elevated sunspot numbers, frequent CME production, organised solar wind stream structure — the heliospheric magnetic field is subject to multiple overlapping disturbances at a variety of temporal and spatial scales. These conditions typically correspond to increased occurrence of ICMEs and persistent co-rotating interaction regions (CIRs),

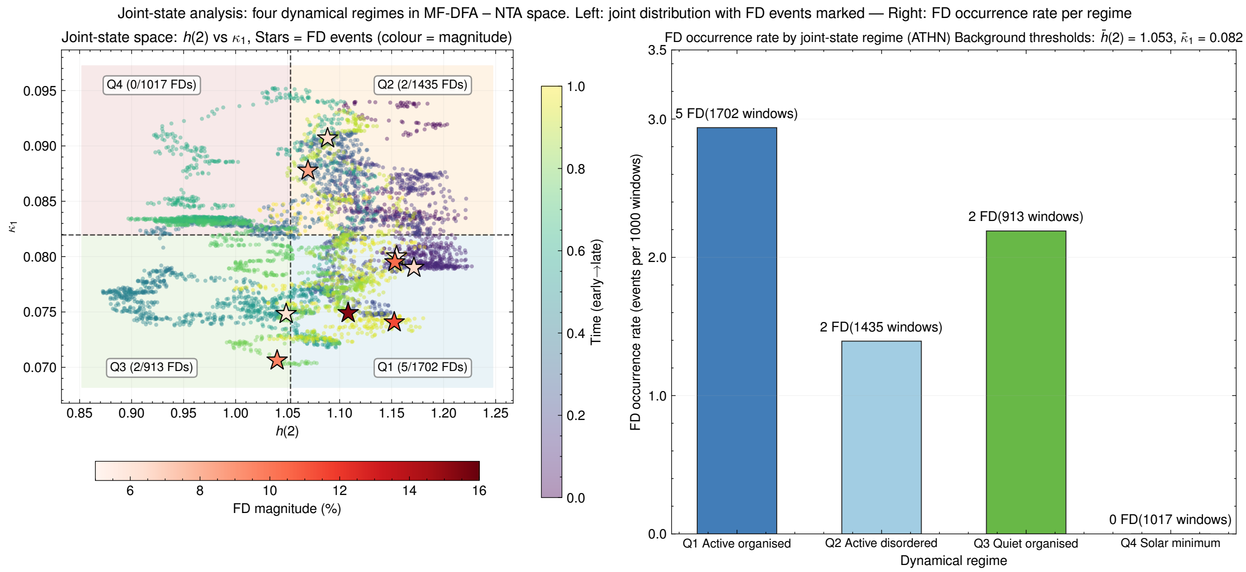

Figure 15: Joint-state analysis in the $h(2)$–κ_1 space (ATHN, 2012–2025). Left: scatter of all 730-day rolling windows coloured by time (purple = early, yellow = recent); the four dynamical regimes are colour-coded by background quadrant; the nine catalogued FD events are marked as stars coloured by magnitude. Dashed lines indicate the background thresholds $h(2)_{\text{bg}}$ and $\kappa_{1,\text{bg}}$. Right: FD occurrence rate (events per 1000 windows) in each regime. Q1 (active organized: high $h(2)$, low κ_1) has the highest rate; Q4 (solar minimum: low $h(2)$, high κ_1) records zero events.

both of which impose structured, multi-scale perturbations on the heliospheric magnetic field. This multi-scale forcing enriches the correlational structure of the CR flux in two complementary ways. First, it enhances long-range persistence: each new disturbance modifies the CRI in a way that is correlated with the previous state of the heliosphere, producing a memory effect that extends across the 730-day window and manifests as elevated $h(2)$. In this context, elevated $h(2)$ reflects a system in which CR fluctuations retain memory of prior heliospheric conditions, rather than evolving as independent or short-memory stochastic variations. Second, it organises the event sequence in natural time: the energy distribution of successive CR fluctuations becomes less uniform and more structured, reducing κ_1 below the uniform-distribution value of 1/12.

The joint-state analysis (Section 3.5.2) quantifies this directly: the regime in which both conditions are met simultaneously (Q1: elevated $h(2)$ and depressed κ_1) shows a FD occurrence rate approximately twice that of the regime where only $h(2)$ is elevated (Q2), and infinitely higher than the solar minimum state (Q4), which records zero large FD events across more than 1000 windows.

The anticorrelation with solar minimum, where both effects reverse, provides strong support for this interpretation: during the 2019–2020 minimum the heliosphere is in its most quiescent state, the CR flux is smooth and weakly modulated, and both $h(2)$ and κ_1 relax toward their respective reference values ($h(2) \to 1$ and $\kappa_1 \to 1/12$).

This picture is consistent with the Kolmogorov–Obukhov scaling of the CR power spectrum reported by Varotsos et al. [33], who showed that the $\gamma = 5/3$ turbulence cascade law governs the CRI time evolution. While the present analysis does not directly measure heliospheric turbulence, the observed scaling behavior is consistent with turbulence-driven transport models of CRs. The elevated $h(2)$ values during active heliospheric periods are consistent with the long-memory tail of such a turbulent cascade: when heliospheric magnetic turbulence is stronger and more organised, the resulting CRs modulation inherits a richer, more persistent correlational structure. The surrogate analysis (Section 3.1.3) provides direct empirical support for this interpretation: at all 16 stations, the observed $\Delta\alpha$ exceeds that of both phase-randomized and AAFT surrogates by $> 30\%$ and with z-scores up to 35, establishing unambiguously that nonlinear long-range correlations — not the shape of the amplitude distribution — drive the multifractal structure of the CR flux.

MF-DFA identifies similar multifractal signatures in atmospheric and geophysical time series, supporting the interpretation of this behavior as stemming from complex, multi-scale dynamical processes [26]. This is precisely the signature expected from a turbulent heliospheric plasma where ICME-driven disturbances, co-rotating interaction regions, and structured magnetic field fluctuations interact nonlinearly across a wide range of temporal scales.

We note, however, that $h(2) \approx 1$ is not uniquely diagnostic of any single mechanism. The same scaling can arise from long-memory stochastic processes such as fractional Gaussian noise [11], from the superposition of multiple modulation processes at different timescales [3], or from non-diffusive transport in a structured heliospheric magnetic field. The surrogate results rule out a purely distributional origin but do not discriminate between these correlation-based mechanisms. The physical process generating the observed $1/f$-type CR scaling with nonlinear multifractal structure remains an open question that motivates theoretical modelling beyond the scope of the present empirical analysis.

4.2 Complementarity of MF-DFA and NTA: an amplitude-scale vs. event-order perspective

The modest correlation between κ_1 and $h(2)$ ($r = 0.117$, $r^2 \approx 1.4\%$) is not a failure of the analysis — it is a result. It quantifies the degree to which two analytically distinct representations of the same physical process are informationally independent. MF-DFA operates in amplitude–scale space: it characterises how the variance of CR fluctuations scales with the temporal window size, and therefore captures the hierarchy of modulation amplitudes across timescales. The Hurst exponent measures persistence, aligning with its application in other geophysical time series analyzed through rescaled range methods [25]. NTA operates in event-order space: it characterises how the energy of successive measurements is distributed relative to their sequential position, and therefore captures the temporal organisation of the event sequence irrespective of the clock-time spacing between events. These two representations are mathematically orthogonal by construction, and the near-zero shared variance confirms that they remain largely orthogonal empirically. The fact that both independently detect the same heliospheric regime — elevated $h(2)$ and depressed κ_1 during active periods — therefore constitutes genuine mutual validation rather than circular confirmation. Each framework provides evidence that the other cannot provide alone, which is precisely what complementarity means in this context.

The joint-state analysis provides a concrete operational illustration of this complementarity: defining the dynamical regime by the intersection of the two thresholds ($h(2) > h(2)_{\rm bg}$ and $\kappa_1 < \kappa_{1,\rm bg}$) produces a sharper discrimination of FD-prone conditions than either threshold alone, because the two criteria capture independent aspects of the heliospheric state.

4.3 The $\Delta\alpha$ signal: window-dependence and regime sensitivity

The decrease in $\Delta\alpha$ observed at Jungfraujoch in the months preceding the two 2024 Forbush events deserves specific discussion in light of its statistical non-generalisability. As noted in Section 3.3, the signal does not reproduce across the full nine-event catalogue, which we interpret as reflecting two compounding factors. First, the signal is window-dependent: because MF-DFA is applied over 730-day windows, a change in $\Delta\alpha$ that begins 120–150 days before the FD onset reflects the gradual narrowing of the multifractal spectrum over the half-year preceding the event, not a local transient. This conditioning requires a sustained period of organised heliospheric forcing — precisely what the extreme solar cycle 25 maximum of 2024 provided — and may not be reproducible in events occurring during less active phases of the cycle. Second, the rigidity-dependence identified in Section 3.3 suggests that the signal is preferentially visible at low-rigidity stations like JUNG, which are more sensitive to the softer component of the primary CR spectrum that responds first to early heliospheric restructuring. At higher rigidities, the signal is suppressed by the energy threshold of the detector.

These considerations point toward a coherent physical picture in which $\Delta\alpha$ is a regime-sensitive rather than event-universal indicator: it responds when the combination of heliospheric activity level and station rigidity places the detector in a configuration where a single dominant modulation scale progressively narrows the multifractal hierarchy. Testing this hypothesis systematically requires a larger event catalogue and, ideally, higher-cadence data.

4.4 Limitations

Several limitations of the present study should be acknowledged. The most important is the size of the FD event catalogue: with $N = 9$ events, the statistical tests have limited power, and the medium effect sizes ($|r| \approx 0.33$–0.38) imply that individual events can swing the results — a caveat that applies equally to the FD rates computed in the joint-state analysis (Section 3.5.2), where Q1 contains only five events. The bootstrap analysis (Section 3.4.3) confirms that the result is stable in the majority of resamples, but a definitive assessment will require a larger catalogue spanning multiple solar cycles at consistent monitoring quality.

A second limitation is the temporal resolution of the analysis. Daily CR data are sufficient to capture the long-term heliospheric regime identified here, but the short-timescale dynamics directly preceding individual FD events — including the NTA signatures reported by Varotsos [7] in the hours before the May 2024 event — require hourly or sub-hourly data. The 730-day rolling window implies that the identified signal reflects long-term heliospheric conditioning rather than short-term dynamics and therefore cannot be used for operational forecasting of individual events.

A third limitation is the choice of the 730-day window length itself. Shorter windows would provide better temporal resolution but reduce the statistical stability of the MF-DFA estimate; longer windows would smooth out event-to-event variability. The 730-day choice is motivated by comparability with Varotsos [7] and by the requirement to fit at least two full solar rotation periods within each window, but the trade-off between resolution and stability is inherent to all sliding-window analyses and cannot be fully resolved without data at finer temporal scales.

4.5 Future directions

The results of this study open several directions for future work. The most immediate is the extension to hourly NMDB data, which would enable a direct comparison between the long-term regime signatures identified here and the short-timescale NTA precursor signals reported by Varotsos [7]. An integrated analysis combining both temporal scales — daily rolling MF-DFA for regime characterisation and hourly NTA for event-level monitoring — could provide a two-tier space weather diagnostic that is more informative than either alone. At hourly resolution, the rolling window could be substantially shortened — potentially to tens of days rather than 730 — while retaining sufficient points per scale for stable MF-DFA fitting, enabling detection of regime transitions on timescales approaching individual solar rotations. This would also permit direct testing of whether the κ_1 values approach the critical threshold 0.070 in the hours before individual events, as reported by

Varotsos [7], rather than only in the long-term 730-day average reported here.

A second direction is the extension of the rigidity analysis to the full 16-station network. The contrast between JUNG and ATHN in the $\Delta\alpha$ response suggests that a systematic study of $\Delta\alpha$ as a function of R_c across all stations and across a larger FD catalogue could clarify the energy-dependent sensitivity of multifractal structure to heliospheric disturbances, and potentially identify optimal rigidity thresholds for $\Delta\alpha$-based monitoring.

Finally, the empirical NTA–MF-DFA bridge established here could be formalised theoretically. The near-orthogonality of the two frameworks in the observed CR data is an empirical fact that calls for a theoretical explanation rooted in the statistical mechanics of CR transport. Understanding why a system with higher $h(2)$ tends also to have lower κ_1 — even weakly — may shed light on the nature of the critical state that NTA identifies and on its relationship to the long-memory processes that MF-DFA quantifies. From an applied standpoint, the heliospheric regime signature identified here may also inform radiation-environment assessments relevant to space-mission planning. Periods classified as Q1 (elevated $h(2)$, depressed κ_1) correspond to heliospheric conditions under which large transient CR modulation events are more likely and could in principle be incorporated as a longer-term contextual indicator alongside existing short-term space weather forecasts, complementing rather than replacing operational warning systems for crewed missions and satellite operations.

5 Conclusions

We have presented the first network-scale, time-resolved multifractal analysis of galactic CRI, combining rolling MF-DFA and rolling NTA applied simultaneously to daily records from 16 NMDB stations over 2010–2025. The principal conclusions are as follows.

1. **Universal persistent long-range correlations.** All 16 stations yield $h(2) > 0.5$, with a network mean $\langle h(2)\rangle = 1.00 \pm 0.09$ consistent with $1/f$-type scaling. Genuine multifractality ($\langle \Delta\alpha\rangle = 1.35 \pm 0.53$) is also universal, with spectral width increasing systematically with geomagnetic cut-off rigidity. These properties are independent of location, altitude, and heliospheric distance from the equatorial plane.

2. **Coherent network-wide solar-cycle modulation.** The rolling MF-DFA heatmap reveals two coherent network-wide decreases in $h(2)$: one during the declining phase of solar cycle 24 (2015–2016) and one during the 2019–2020 solar minimum. Both are visible simultaneously at all latitudes and rigidities, confirming that the multifractal structure of CRI is globally driven by heliospheric conditions rather than by local or detector-specific effects.

3. **A heliospheric regime signature of large Forbush decreases.** Across nine major FD events ($> 6\%$, 2011–2024), $h(2)$ at ATHN is above background in 7/9 cases (Mann–Whitney $p = 0.025$, $r = -0.378$) and κ_1 is below background in 7/9 cases ($p = 0.041$, $r = -0.335$). Bootstrap resampling confirms that 66% and 56% of resamples yield $p < 0.05$ respectively, establishing that the result is not driven by any single event. This joint signature, detected independently by MF-DFA and NTA, characterises a distinct heliospheric dynamical regime associated with sustained solar activity rather than providing a quantitative precursor of individual FD amplitudes.

4. **Apparent precursor in $\Delta\alpha$ at Jungfraujoch.** For the two extreme 2024 FD events, $\Delta\alpha$ at Jungfraujoch decreases systematically 120–150 days before onset ($\sim$20–27% below baseline). This behaviour is physically interpretable in terms of the rigidity-dependent sensitivity of low-R_c stations to early heliospheric restructuring, but does not generalise across the full

nine-event catalogue. It constitutes an illustrative signal that motivates further investigation rather than a demonstrated general precursor.

5. **Complementarity of MF-DFA and NTA.** The empirical correlation between κ_1 and $h(2)$ ($r = 0.117$, $r^2 \approx 1.4\%$) confirms that the two frameworks capture predominantly independent aspects of CR dynamics: MF-DFA characterises the amplitude-scale hierarchy of fluctuations, while NTA characterises the energy ordering of the event sequence. Their independent detection of the same heliospheric regime constitutes mutual validation and demonstrates that their joint application provides a more complete diagnostic of the heliospheric state than either framework alone.

Together, these results establish a new methodological framework for the multi-scale characterisation of CR dynamics at the network scale, and provide an empirical foundation for future work integrating daily regime analysis with sub-daily event monitoring in a unified space weather diagnostic system.

Acknowledgments

The authors thank the neutron monitor stations contributing to the Neutron Monitor Database (NMDB; https://www.nmdb.eu) for making their data publicly available in real time. We are grateful to the station teams at Athens, Jungfraujoch, Oulu, Apatity, and all other NMDB contributing institutions for maintaining continuous, high-quality CRs records over the 2010–2025 period analysed here. This work was based on the findings of the completed IAA Study (1.16) entitled: "Nowcasting Extreme Cosmic Ray Events." D.S.-P. acknowledges support from the Universidad Tecnológica de Bolívar (UTB), Escuela de Transformación Digital, Cartagena de Indias, Colombia.

Data Availability

All CRI data used in this study are publicly available through the Neutron Monitor Database at https://www.nmdb.eu. The analysis code — including the rolling MF-DFA and NTA pipelines, surrogate tests, and figure-reproduction notebooks — is available at https://github.com/sierraporta/CT-multifractal-NTA-Network. Derived data products (rolling metric tables, surrogate distributions) are included in the repository.

References

[1] E. N. Parker. The passage of energetic charged particles through interplanetary space. *Planetary and Space Science*, 13(1):9–49, 1965. doi: 10.1016/0032-0633(65)90131-5.

[2] J. S. Rankin, V. Bindi, A. M. Bykov, A. C. Cummings, S. Della Torre, V. Florinski, B. Heber, M. S. Potgieter, E. C. Stone, and M. Zhang. Galactic cosmic rays throughout the heliosphere and in the very local interstellar medium. *Space Science Reviews*, 218(5):42, 2022. doi: 10.1007/s11214-022-00912-4.

[3] N. E. Engelbrecht, F. Effenberger, V. Florinski, M. S. Potgieter, D. Ruffolo, R. Chhiber, A. V. Usmanov, J. S. Rankin, and P. L. Els. Theory of cosmic ray transport in the heliosphere. *Space Science Reviews*, 218(4):33, 2022. doi: 10.1007/s11214-022-00896-1.

[4] H. V. Cane. Coronal mass ejections and forbush decreases. *Space Science Reviews*, 93(1):55–77, 2000. doi: 10.1023/A:1026532125747.

[5] I. G. Richardson and H. V. Cane. Galactic cosmic ray intensity response to interplanetary coronal mass ejections/magnetic clouds in 1995–2009. *Solar Physics*, 270(2):609–627, 2011. doi: 10.1007/s11207-011-9774-x.

[6] A. A. Melkumyan, A. V. Belov, M. A. Abunina, A. A. Abunin, N. S. Shlyk, V. A. Oleneva, and V. G. Yanke. Forbush decreases associated with coronal mass ejections from active and non-active regions: statistical comparison. *Monthly Notices of the Royal Astronomical Society*, 515(3):4430–4444, 2022. doi: 10.1093/mnras/stac2017.

[7] C. Varotsos. The hidden order of cosmic rays: Fractal scaling and temporal complexity. *Fractal and Fractional*, 9(11):748, 2025. doi: 10.3390/fractalfract9110748.

[8] J. Kirkby, J. Curtius, J. Almeida, E. Dunne, J. Duplissy, S. Ehrhart, A. Franchin, S. Gagné, L. Ickes, A. Kürten, et al. Role of sulphuric acid, ammonia and galactic cosmic rays in atmospheric aerosol nucleation. *Nature*, 476(7361):429–433, 2011. doi: 10.1038/nature10343.

[9] C. Varotsos, J. Ondov, C. Tzanis, F. Öztürk, M. Nelson, H. Ke, and J. Christodoulakis. An observational study of the atmospheric ultra-fine particle dynamics. *Atmospheric Environment*, 59:312–319, 2012. doi: 10.1016/j.atmosenv.2012.05.015.

[10] C. Tzanis, C. Varotsos, M. Ferm, J. Christodoulakis, M. N. Assimakopoulos, and C. Efthymiou. Nitric acid and particulate matter measurements at athens, greece, in connection with corrosion studies. *Atmospheric Chemistry and Physics*, 9(21):8309–8316, 2009. doi: 10.5194/acp-9-8309-2009.

[11] B. B. Mandelbrot. *The fractal geometry of nature/Revised and enlarged edition*. San Francisco : W.H. Freeman, New York, 1983. ISBN 978-0716711865.

[12] C. A. Varotsos, G. S. Golitsyn, M. Efstathiou, and N. Sarlis. A new method of nowcasting extreme cosmic ray events. *Remote Sensing Letters*, 14(6):576–584, 2023. doi: 10.1080/2150704X.2022.2057204.

[13] C. A. Varotsos, G. S. Golitsyn, Y. Xue, M. Efstathiou, N. Sarlis, and T. Voronova. On the relation between rain, clouds, and cosmic rays. *Remote Sensing Letters*, 14(3):301–312, 2023. doi: 10.1080/2150704X.2023.2190468.

[14] J. Christodoulakis, C. A. Varotsos, H. Mavromichalaki, M. N. Efstathiou, and M. Gerontidou. On the link between atmospheric cloud parameters and cosmic rays. *Journal of Atmospheric and Solar-Terrestrial Physics*, 189:98–106, 2019. doi: 10.1016/j.jastp.2019.04.012.

[15] G. Golitsyn and C. Varotsos. *The Stochastic Nature of Environmental Phenomena and Processes*. Springer, Berlin/Heidelberg, Germany, 2025. ISBN 978-3-031-77014-2. doi: 10.1007/978-3-031-77015-9.

[16] L. F. Gomes, T. F. P. Gomes, E. L. Rempel, and Sílvio Gama. Origin of multifractality in solar wind turbulence: the role of current sheets. *Monthly Notices of the Royal Astronomical Society*, 519(3):3623–3634, 2023. doi: 10.1093/mnras/stac3577.

[17] E. K. J. Kilpua, S. Good, M. Ala-Lahti, A. Osmane, and V. Koikkalainen. Permutation entropy and complexity analysis of large-scale solar wind structures and streams. *Annales Geophysicae*, 42(1):163–177, 2024. doi: 10.5194/angeo-42-163-2024.

[18] C-K Peng, S. V. Buldyrev, S. Havlin, M. Simons, H. E. Stanley, and A. L. Goldberger. Mosaic organization of dna nucleotides. *Physical review e*, 49(2):1685, 1994. doi: 10.1103/PhysRevE.49.1685.

[19] J. W. Kantelhardt, S. A Zschiegner, E. Koscielny-Bunde, S. Havlin, A. Bunde, and H. E. Stanley. Multifractal detrended fluctuation analysis of nonstationary time series. *Physica A: Statistical Mechanics and its Applications*, 316(1-4):87–114, 2002. doi: 10.1016/S0378-4371(02)01383-3.

[20] D. Sierra-Porta. On the fractal properties of cosmic rays and sun dynamics cross-correlations. *Astrophysics and Space Science*, 367(12):116, 2022. doi: 10.1007/s10509-022-04151-5.

[21] D. Sierra-Porta. Multifractal detrended cross-correlation coefficient for cosmic ray and sunspot time series. *Journal of Atmospheric and Solar-Terrestrial Physics*, 266:106407, 2025. doi: 10.1016/j.jastp.2024.106407.

[22] D. Sierra-Porta. Relationship between magnetic rigidity cutoff and chaotic behavior in cosmic ray time series using visibility graph and network analysis techniques. *Chaos: An Interdisciplinary Journal of Nonlinear Science*, 34(2), 2024. doi: 10.1063/5.0167156.

[23] A. Giri, B. Adhikari, S. Dahal, K. S. S. Paula, and M. J. A. Bolzan. Multi-fractal analysis of cosmic rays over mid-and high-latitude stations during severe geomagnetic storms. *Solar Physics*, 299(10):148, 2024. doi: 10.1007/s11207-024-02393-w.

[24] R. Modzelewska, A. Krasińska, A. Wawrzaszek, and A. Gil. Scaling features of diurnal variation of galactic cosmic rays. *Solar Physics*, 296(8):125, 2021. doi: 10.1007/s11207-021-01866-6.

[25] S. Pal, S. Dutta, T. Nasrin, and S. Chattopadhyay. Hurst exponent approach through rescaled range analysis to study the time series of summer monsoon rainfall over northeast india: S. pal et al. *Theoretical and Applied Climatology*, 142(1):581–587, 2020. doi: 10.1007/s00704-020-03338-6.

[26] S. Chakraborty and S. Chattopadhyay. A probe into the behaviour of total ozone time series through multifractal detrended fluctuation analysis. *Theoretical and Applied Climatology*, 148 (1):671–677, 2022. doi: 10.1007/s00704-022-03967-z.

[27] S. Chattopadhyay and G. Chattopadhyay. Conjugate gradient descent learned ann for indian summer monsoon rainfall and efficiency assessment through shannon-fano coding. *Journal of Atmospheric and Solar-Terrestrial Physics*, 179:202–205, 2018. doi: 10.1016/j.jastp.2018.07.015.

[28] N. Acharya, S. Chattopadhyay, M. A Kulkarni, and U. C. Mohanty. A neurocomputing approach to predict monsoon rainfall in monthly scale using sst anomaly as a predictor. *Acta Geophysica*, 60(1):260–279, 2012. doi: 10.2478/s11600-011-0044-y.

[29] G. Chattopadhyay and S. Chattopadhyay. A probe into the chaotic nature of total ozone time series by correlation dimension method. *Soft computing*, 12(10):1007–1012, 2008. doi: 10.1007/s00500-007-0267-7.

[30] M. Echim, C. Munteanu, G. Voitcu, and E. Teodorescu. Solar wind turbulence and complexity probed with rank-ordered multifractal analysis (roma). *Entropy*, 26(11):929, 2024. doi: 10.3390/e26110929.

[31] C. A. Varotsos, C. L. E. Franzke, M. N. Efstathiou, and A. G. Degermendzhi. Evidence for two abrupt warming events of sst in the last century. *Theoretical and Applied Climatology*, 116 (1):51–60, 2014. doi: 10.1007/s00704-013-0935-8.

[32] P. Varotsos, N. Sarlis, and E. Skordas. *Natural Time Analysis: The New View of Time, Part II: Advances in Disaster Prediction Using Complex Systems*. Springer Nature, 1 edition, 2023. ISBN 978-3-031-26005-6. doi: 10.1007/978-3-031-26006-3.

[33] C. A. Varotsos, G. S. Golitsyn, Y. Mazei, N. V. Sarlis, Y. Xue, H. Mavromichalaki, and M. N. Efstathiou. On the observed time evolution of cosmic rays in a new time domain. *Acta Astronautica*, 225:436–443, 2024. doi: 10.1016/j.actaastro.2024.09.034.

[34] N. V. Sarlis, E. S. Skordas, S.-R. G. Christopoulos, and P. A. Varotsos. Natural time analysis: The area under the receiver operating characteristic curve of the order parameter fluctuations minima preceding major earthquakes. *Entropy*, 22(5):583, 2020. doi: 10.3390/e22050583.

[35] A. Ramírez-Rojas, E. L. Flores-Márquez, N. V. Sarlis, and P. A. Varotsos. The complexity measures associated with the fluctuations of the entropy in natural time before the deadly méxico m8. 2 earthquake on 7 september 2017. *Entropy*, 20(6):477, 2018. doi: 10.3390/e20060477.